

POLITECNICO DI TORINO

Master's Degree in Electrical Engineering



**Politecnico
di Torino**

Master's Degree Thesis

**Integrated drive for high-power
alternating bidirectional electric vehicles
charging: the EMC issuers, simulations,
design and tests.**

Supervisor

Prof. Paolo GUGLIELMI

Candidate

Alessia ANSALDI

July 2024

Summary

The ecological transition is a pivotal concern in today's world, with decarbonisation being one of the most pressing challenges. The goal is to reduce emissions by 33 % by 2030 and achieve carbon neutrality by 2050. A significant contributor to emissions is the private transport sector, responsible for 71.7 % of carbon dioxide emissions in Europe. This necessitates a transition from combustion engine vehicles to electric vehicles (EVs).

This thesis focuses on the safety issues related to parasitic capacitances and electromagnetic compatibility (EMC) in EV charging systems. Parasitic capacitances in electric motors, particularly in modern high-frequency and high-speed applications, are a significant concern. These unwanted capacitances arise from the physical structure and spatial arrangement of the motor components, leading to performance and reliability issues. The high-frequency switching actions of modern inverters generate voltage components with high dv/dt , which can excite the parasitic capacitances within the motor, causing high-frequency currents that lead to additional power losses and excessive heating. This heating degrades insulation materials over time, leading to premature insulation failure and reduced motor lifespan. Moreover, these currents can lead to EMC issues, disrupting the operation of electrical devices through signal coupling, noise generation, and impedance mismatch.

A potential solution is to use a nine-phase machine that allows three-phase charging without hardware reconfiguration, thereby reducing costs and avoiding torque generation during the charging process. This machine, specifically a Permanent Magnet Synchronous Motor (PMSM) with five pole pairs, offers higher torque density and efficiency compared to induction motors.

The multi-phase motor's structure not only aids in simple limp-home mode realization but also reduces stress on components, enabling the use of more economical devices. This thesis includes the examination of a nine-phase machine and its assembly, with a particular design of the inverter functioning as a rectifier during battery charging.

The introduction chapter outlines the current methods of vehicle charging and European legislation. Following this, an analysis of torque generation during the charging phase is presented, emphasizing the importance of zero torque to prevent vehicle movement during charging. The high-frequency motor model developed in Chapter 3 aims to match real motor behavior through simulations. Chapter 4 delves into the study of parasitic capacitances in the motor, including a section on dielectric losses in the cooling system. The final chapter discusses the assembly of the motor prototype.

This research underscores the importance of understanding and mitigating parasitic capacitances and EMC issues to enhance the safety and efficiency of integrated on-board EV chargers, contributing to more reliable and sustainable electric vehicle technologies

Acknowledgements

Scrivere questa tesi è stato un viaggio impegnativo e gratificante, reso possibile solo grazie al sostegno e all'incoraggiamento di molte persone. Ogni fase di questo percorso ha richiesto impegno, dedizione e supporto, e desidero esprimere la mia sincera gratitudine a coloro che mi hanno accompagnato e sostenuto lungo la strada.

Ai miei genitori: Non esistono parole sufficienti per esprimere la mia gratitudine. Mi avete sempre incoraggiato a seguire i miei sogni e mi avete fornito tutto il necessario per raggiungerli. Se vogliamo dirlo diversamente vi ringrazio anche per essere stati i principali finanziatori di questa mia impresa. Grazie **Mamma** per gli esaurimenti al suono di "ma stai studiando?" e grazie **Papà** perchè so che ancora sei convinto che Genova mi sarebbe piaciuta.

A mio fratello: Grazie per il tuo supporto e per essere sempre presente nei momenti di bisogno, ma soprattutto grazie per aver distolto almeno ogni tanto l'attenzione di quella rompiscatole di nostra madre dal mio percorso permettendomi di respirare.

Ai miei amici, vecchi e nuovi, e ai miei colleghi: Grazie per essere stati al mio fianco durante tutto questo percorso, condividendo sia i momenti di gioia che quelli di difficoltà. Grazie a chi mi è accanto dall'inizio del percorso e a chi ho conosciuto lungo la via. La vostra amicizia è una fonte inesauribile di conforto e ispirazione. C'è però qualcuno che merita una menzione speciale: **Dario**, ci conosciamo da troppi anni, sei assolutamente l'amico più datato presente oggi, forse dovrei ringraziarti per avermi sopportata così a lungo. **Sara**, ormai siamo praticamente sposate, e un matrimonio ha i suoi pro e i suoi contro. Cercavo una coinquilina e ho trovato un'amica, spero di poter continuare a parlare di tutto e tutti con te ancora a lungo. **Marco**, o dovrei dire papy, sei il fratello maggiore che tutti vorremmo (o almeno di cui avremmo bisogno), una fonte inesauribile di buoni consigli e un pessimo ballerino di salsa. Senza di te il mio percorso non sarebbe stato lo stesso, letteralmente. **Chiara**, una collega che è diventata molto di più, forse però poteva succedere prima! Vorrei condividere per sempre con te le gioie e soprattutto i malesseri che questa vita ci dona. **Giulio**, una scoperta tutto sommato recente, il mio salsa bro e confidente, grazie per le ore passate a

sopportare i miei sproloqui. **Marco**, troppi progetti e troppi scleri passati insieme, ti ringrazio per la tua calma infinita ma sta pur certo che non ti stai liberando di me.

Potrei continuare all'infinito ma non basterebbero le pagine di questa tesi, quindi un enorme "Grazie" a tutti.

Ai ricercatori e ai dottorandi del DENERG: Desidero ringraziarvi per la vostra collaborazione, il vostro aiuto e i vostri preziosi consigli. Lavorare insieme a voi è stato un privilegio e un'esperienza di crescita professionale e personale. In particolare grazie a **Fausto** e ai suoi inverter, a **Simone** per i pettegolezzi, ma non solo, a **Stefano** che mi ha salvata da Ansys e soprattutto a **Enrico**, ora che sono uscita dal laboratorio potrà finalmente tirare un sospiro di sollievo.

Al Team H_2 politO: È stato un onore far parte di un gruppo così dinamico e motivato. La nostra collaborazione ha arricchito la mia esperienza universitaria e ha contribuito significativamente alla mia formazione. Grazie per il vostro impegno, la vostra creatività e la vostra amicizia. Insieme, abbiamo raggiunto traguardi che da soli non avremmo mai potuto immaginare e condiviso sciagure ancora più inimmaginabili. Un grazie particolare alla professoressa **Massimiliana Carello** che, soprattutto nel mio anno da Team Leader, mi ha insegnato il significato della parola "tenacia".

Al mio relatore: Un ringraziamento speciale va al mio relatore, professor **Paolo Guglielmi**. La sua guida, il suo supporto e i suoi consigli preziosi sono stati fondamentali per la realizzazione di questa tesi. Grazie per avermi seguito con dedizione e pazienza, ma anche per aver lasciato che mi arrangiassi, aiutandomi a superare le difficoltà e a crescere sia a livello accademico che personale.

Infine, vorrei esprimere la mia profonda gratitudine a tutti coloro che, in un modo o nell'altro, hanno contribuito a questo progetto. Senza di voi, questo lavoro non sarebbe stato possibile.

Grazie di cuore a tutti.

“Dormire è sopravvalutato”
Somebody

Table of Contents

List of Tables	XI
List of Figures	XII
Acronyms	XVI
1 Introduction	1
1.1 Aim of the Thesis	2
1.1.1 High Switching Frequency Motor Model	2
1.1.2 Parasitic Capacitances in the Motor	4
1.2 Overview of Charging Columns Legislation and Actual Standards	6
1.2.1 Charging Columns and Connectors	6
1.2.2 Current International Situation	9
1.2.3 Power Cables	10
1.2.4 Conclusions on Charging Modes and Connectors	10
1.3 Parasitic Currents Standards	10
1.4 Motor Structure	12
1.5 Integrated On-Board Battery Charger	14
1.5.1 Grid Supply	17
1.5.2 Battery Specifics	17
1.5.3 Switches Selection	20
2 Preliminary Verification of the Presence of Null Torque during Charging	22
2.1 FEM 2D Simulations	24
2.1.1 Introduction to Finite Element Analysis (FEA) and Finite Element Method (FEM)	24
2.1.2 2D Motor Simulation	24
2.2 MATLAB Script to identify Synchronous Harmonics	27
2.3 Experimental Setup and Results	29

3	High Frequency Motor Model	34
3.1	Lumped HF Parameters First Measurement	35
3.1.1	Further Considerations on Winding-to-Housing Capacitance C_g	37
3.2	PLECS First Draft Simulation	37
3.2.1	Total Current flowing in the Motor Housing	38
3.2.2	Voltage between motor housing and ground	39
3.3	HF Motor Model Sweep Measurements	40
3.3.1	Impedance Measurements for each of the Nine Phases	40
3.3.2	Impedance Measurements for One Phase and Different Rotor Positions	43
3.3.3	3D Model of the Measurements, One Phase and Different Rotor Positions	46
3.4	Approximated Model for PLECS Simulations using Passive Compo- nents based on Sweep Impedance Measurements and Foster Form .	47
3.4.1	Phase - to - Star center Impedance	49
3.4.2	Phase - to - Housing Impedance	51
3.4.3	Star center - to - Housing Impedance	54
3.5	Conclusion oh High Frequency Motor Model	57
4	ANSYS motor model	58
4.1	Ansyz Maxwell Introduction	59
4.2	Finite Element Analysis (FEA) Method and Energy Error	60
4.3	Parasitic Capacitances Evaluation	61
4.3.1	First Model of the Motor	61
4.3.2	Cool-X Motor Model	64
4.3.3	Complete Motor Model	65
4.4	Dielectric Losses in Cool-X Device	66
4.4.1	Dielectric Properties of Ethylene Glycol 50% Solution	67
4.4.2	Dielectric Properties of Other Commercial Coolants	67
4.4.3	Dielectric Losses Evaluation for a 50% Ethylene Glycol Solu- tion and Comparison with Other Coolants	68
5	Assembly of a Liquid-Cooled Motor Version (Cool-X)	70
5.1	Insulation Test	70
5.2	Connection of the Three Star Centers and Winding-to-Cool-X Con- nection	71
5.3	Experimental Tests on the Motor	73
5.3.1	Common Mode Configuration to Evaluate the Parasitic Ca- pacitances	73

6	Conclusions	75
6.1	Summary of Findings	75
6.2	Implications for Future Research and Applications	76
6.3	Conclusion	76
A	MATLAB convolution product script	77
B	Mylar Datasheet	79
C	MATLAB Bode plot approximation script, phase-to-star center impedance	80
D	MATLAB Bode plot approximation script, phase-to-housing impedance	83
E	MATLAB Bode plot approximation script, star center-to-housing impedance	86
	Bibliography	89

List of Tables

1.1	Charging modes definitions	6
1.2	Charging types Mode 3	8
1.3	Motor data	13
1.4	Peak and rms maximum and minimum voltage values	17
1.5	LFP and NMC cells comparison	19
2.1	Direct voltage and current measurements	32
3.1	HF lumped motor parameters	37
4.1	Stator and concentrated windings parasitic capacitances	62
4.2	Parasitic capacitances considering Cool-X device	66
4.3	Dielectric losses in Cool-X devices using different coolants	69

List of Figures

1.1	New registrations of electric vehicles in Europe from 2010 to 2022 [2]	1
1.2	Charging Mode 1	7
1.3	Charging Mode 2	7
1.4	Charging Mode 3	8
1.5	Charging Mode 4	9
1.6	Connectors types	9
1.7	First draft and final prototype motor section	13
1.8	Phase displacement between the terns	13
1.9	Motor components	14
1.10	On-board vs off-board chargers	15
1.11	Simple system scheme	15
1.12	Electrical scheme	16
1.13	Equivalent charging scheme	16
1.14	Grid-to-battery undesired current	18
1.15	LFP vs NMC cells	19
1.16	Si, SiC and GaN devices comparison	20
1.17	Power capability versus switching frequency for popular high-voltage, high-current transistors and other devices, as well as primary appli- cations	21
2.1	FEMM 4.2 simulation plot	24
2.2	Grid 3-phase supply	25
2.3	Torque generated for different rotor positions	25
2.4	Three-case comparison	26
2.5	Considered points of phase 1 current	26
2.6	Torque generated for different moments and rotor positions	27
2.7	Detail of the torque generated for different moments and rotor positions	27
2.8	MATLAB plot showing distributions and synchronous harmonics	28
2.9	MATLAB plot detail of low amplitude synchronous harmonics	29
2.10	Phase-to-phase insulation test	29
2.11	Autotransformer scheme	30

2.12	Autotransformer that reproduces the grid	30
2.13	Full wave three-phase rectifier waveforms	31
2.14	Filtered line current	31
2.15	Resistors bench	32
2.16	Test setup scheme	32
2.17	Test setup electrical scheme	33
2.18	Experimental setup with diode rectifier and resistive load	33
3.1	RLE one phase motor model	35
3.2	Connection layout for the phase-to-housing impedance measurements	35
3.3	Hioki 3536 LCR meter	36
3.4	Single-phase HF equivalent circuit	36
3.5	Complete HF inverter leg and motor model with analitically calcu- lated impedances	38
3.6	HF model with amperometers	39
3.7	Voltage oscillations setup and plot	39
3.8	Phase-to-star center impedance, module and phase	40
3.9	Phase-to-housing impedance, module and phase	41
3.10	Star center-to-housing impedance, module and phase	42
3.11	Phase-to-star center impedance, module and phase	43
3.12	Phase-to-housing impedance, module and phase	44
3.13	Star center-to-housing impedance, module and phase	45
3.14	Phase-to-housing impedance 3D, module and phase	46
3.15	Phase-to-star center impedance 3D, module and phase	47
3.16	Phase-to-star center Impedance, experimental data and approximation	50
3.17	Phase-to-housing Impedance, experimental data and approximation	52
3.18	Star center-to-housing Impedance, experimental data and approxi- mation	55
3.19	High frequency motor model for PLECS simulation	57
4.1	Parasitic capacitances schematic	58
4.2	CAD design of the motor	59
4.3	Stator and insulated windings motor model	62
4.4	Mesh of the motor model	63
4.5	Mesh detail	64
4.6	Cool-X device	64
4.7	Motor model including Cool-X devices	65
4.8	Complete motor model	66
4.9	FEMM 4.2 simulation complete setup for dielectric losses evaluation	68
4.10	FEMM 4.2 simulation simplified setup for dielectric losses evaluation	69
5.1	1000 V insulation test on the motor	71

5.2	Windings-to-Cool-X connection	72
5.3	Star-center connection	72
5.4	Motor connected to the nine-phase inverter	73
5.5	Experimental setup	74
5.6	Common mode voltage and current (expanded)	74

Acronyms

AC

Alternating Current

DC

Direct Current

EMC

Electromagnetic Compatibility

EV

Electric Vehicle(s)

EVSE

Electric Vehicle Supply Equipment

FEM

Finite Element Method

GaN

Gallium Nitride transistors

HF

High Frequency

LFP

lithium iron phosphate

NMC

lithium nickel manganese cobalt oxide

PMSM

Permanent Magnet Synchronous Motor

SAE

Society of Automotive Engineers

SiC

Silicon Carbide MOSFETs

VSI

Voltage Source Inverter

Chapter 1

Introduction

The transport sector is among the largest contributors to EU greenhouse gases emissions. Therefore, reducing transport emissions has a key role to meet EU's climate neutrality objectives. The ever-increasing demand for electric vehicles are taking the market in a direction that will face an increasing increase in the sale of electric vehicles.

The decrease in the price of electric vehicles promised by carmakers by 2025 [1] will contribute to the increase in the spread of electric vehicles replacing vehicles equipped with internal combustion engines.

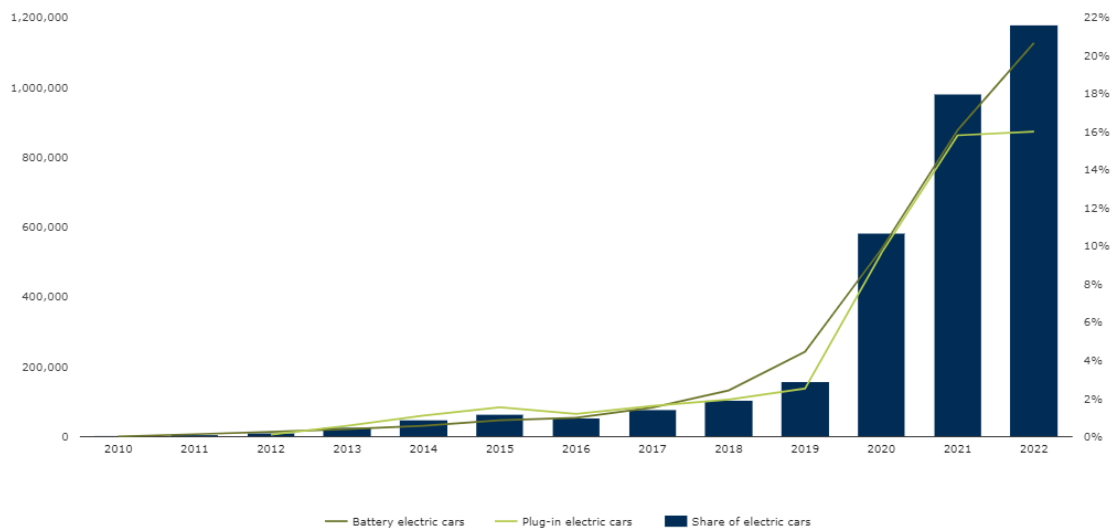


Figure 1.1: New registrations of electric vehicles in Europe from 2010 to 2022 [2]

This introductory chapter is intended primarily to give an overview of the current methods of charging vehicles, as well as the current european law.

A chapter dedicated to the study of the torque generated during the charging phase follows. This analysis could seem trivial but the torque generation during charging phase can represent a problem of no little account, since it is clear that during the charging phase the vehicle must stand still.

Next, an high frequency motor model has been produced in chapter 3 to be used in PLECS simulations to better match the real motor behavior.

Chapter 4 focuses on the study of parasitic capacitances in the studied motor, with in addition a small section dedicated to the study of dielectric losses in the in-cave cooling system.

To end up, last chapter deals with the assembly of the studied motor. In fact, this prototype was developed years ago but it was never assembled.

1.1 Aim of the Thesis

The main objective of this thesis is to investigate the possibility of using the components already present in the vehicle during the drive (motor and inverter) to carry out the battery charging phase, with a special focus on safety issues. This solution would reduce costs by reducing the number of components needed in the vehicle, but brings some critical issues that can not be neglected.

A particular type of motor will be used for this: it is a synchronous multi-phase permanent magnet machine. In particular it is a multi-three-phase motor, with a total of nine phases grouped into three stars. This particular configuration allows to exploit the star centers to realize the three-phase or single-phase recharging by not introducing a torque generated by the windings. The motor pairs with a special nine-phase floating inverter.

The particular configuration of the system motor+inverter brings to the possibility of having higher circulating parasitic currents in the motor housing. For this reason the thesis will focus on the parasitic capacitances study.

1.1.1 High Switching Frequency Motor Model

High switching frequency electric motor models are increasingly prevalent in advanced motor control applications, offering significant benefits in performance, efficiency, and control precision. However, the adoption of high switching frequencies introduces several challenges and potential issues that must be meticulously

addressed to ensure reliable operation and longevity of the motor systems.

One of the primary benefits of high switching frequency is the improved dynamic response and reduced torque ripple. This results from the more frequent updates to the motor's drive signals, allowing for smoother and more precise control of the motor's electromagnetic torque. Additionally, higher switching frequencies enable the use of smaller passive components, such as inductors and capacitors, leading to more compact and lightweight motor drive systems.

Despite these advantages, high switching frequencies can lead to significant issues, primarily associated with electromagnetic interference (EMI), bearing currents, and thermal management challenges. EMI is a critical concern as higher switching speeds generate more high-frequency noise, which can interfere with nearby electronic equipment and degrade the performance of the motor drive system itself. Effective EMI mitigation strategies, such as improved shielding, filtering, and layout design, are essential to manage these emissions.

Bearing currents pose a significant challenge in high switching frequency applications. The rapid voltage changes at high frequencies can induce high-frequency currents in the motor windings and bearings. These currents can lead to premature bearing failures due to electrical discharge machining (EDM) effects, causing pitting and fluting in the bearing surfaces. This issue is exacerbated by the increased switching frequency, which heightens the likelihood and intensity of these harmful currents.

Mitigating bearing currents requires a multifaceted approach. Implementing appropriate insulation materials and bearing designs is crucial to withstand the high-frequency stresses. Additionally, the use of grounding techniques, such as shaft grounding brushes or insulated bearings, can effectively divert harmful currents away from the bearings. Filters and common-mode chokes are also employed to reduce the high-frequency components that contribute to bearing currents.

Thermal management also becomes more challenging at higher switching frequencies. The increased power losses generate additional heat, which must be effectively dissipated to prevent overheating and ensure the reliability of the motor and drive components. Advanced cooling techniques, such as liquid cooling and improved heat sink designs, are often necessary to manage the thermal load in high-frequency switching applications.

In summary, while high switching frequency electric motor models offer substantial performance benefits, they also pose significant technical challenges, particularly

regarding bearing currents. Addressing these issues requires a comprehensive approach involving advanced EMI mitigation, optimized power electronics design, effective thermal management, and robust motor and drive component selection. Ensuring these aspects are adequately managed is crucial for the successful deployment of high switching frequency motor systems in demanding applications.

1.1.2 Parasitic Capacitances in the Motor

Parasitic capacitances in electric motors are a significant concern, particularly in modern high-frequency and high-speed applications. These unwanted capacitances arise from the physical structure and spatial arrangement of the motor components, leading to various performance and reliability issues. Understanding and mitigating these effects are crucial for enhancing motor efficiency and longevity.

Parasitic capacitances in electric motors can be broadly categorized into three types: stator-to-rotor capacitance, winding-to-winding capacitance, and winding-to-frame capacitance. The stator-to-rotor capacitance occurs between the stator windings and the rotor, typically through the air gap. This type of capacitance is influenced by the dielectric properties of the air and the geometry of the motor components. Winding-to-winding capacitance arises between the turns of the windings, which is primarily a function of the winding layout and the insulation materials used. Winding-to-frame capacitance exists between the windings and the motor frame, affected by the proximity and orientation of the windings to the frame .

In inverter-fed motors, the issue of parasitic capacitances becomes more pronounced. The high-frequency switching actions of modern inverters generate voltage components with high dv/dt (rate of change of voltage), which can excite the parasitic capacitances within the motor. These capacitances provide pathways for high-frequency currents, leading to several adverse effects. One significant issue is the circulation of high-frequency currents within the motor windings and components, which can result in additional power losses and excessive heating. This heating can degrade the insulation materials over time, leading to premature insulation failure and reduced motor lifespan .

Another critical issue related to parasitic capacitances is the generation of stray currents. These currents can lead to EMC issues. EMC issues arise when electromagnetic interference (EMI) disrupts the operation of electrical devices. This interference can come from external sources or be generated internally by the vehicle's own systems. Common EMC issues include signal degradation, increased noise levels, and failure of electronic components to operate correctly. How Parasitic

Capacitances and Currents Lead to EMC Problems:

- **Signal Coupling:** Parasitic capacitances can cause signals to couple between different parts of the circuit, leading to crosstalk and interference. This unintended coupling can generate noise that affects sensitive components, causing EMC problems.
- **Noise Generation:** Parasitic currents, induced by parasitic capacitances, can create electromagnetic fields that radiate noise. This noise can interfere with other components and systems within the vehicle, leading to EMC issues.
- **Impedance Mismatch:** Parasitic capacitances can cause impedance mismatches in high-frequency circuits, leading to signal reflections and degradation. This can affect the integrity of communication signals, causing EMC problems.

To mitigate the effects of parasitic capacitances, several strategies can be employed. Shielding techniques, such as the use of conductive barriers or grounded metallic layers, can help to redirect high-frequency currents away from sensitive components. The selection of insulation materials with appropriate dielectric properties is also crucial. These materials should have high dielectric strength and low dielectric loss to minimize the impact of high-frequency currents. Additionally, optimizing the physical layout of the motor components can reduce the parasitic capacitances. For example, increasing the air gap between the stator and rotor or modifying the winding configuration can help to minimize capacitive coupling .

Advanced simulation tools and modeling techniques play a vital role in predicting and mitigating the effects of parasitic capacitances. Finite element analysis (FEA) and other computational methods can be used to model the electromagnetic fields and identify potential issues during the design phase. These tools allow engineers to optimize the motor design and materials to reduce the impact of parasitic capacitances before physical prototypes are built .

Research in this area continues to advance, with ongoing efforts to develop better materials and design methodologies to address the challenges posed by parasitic capacitances. Understanding and managing these capacitances are essential for improving the reliability, efficiency, and performance of electric motors, particularly in demanding applications. [3]

1.2 Overview of Charging Columns Legislation and Actual Standards

This discussion begins with an overview of current legislation and standards related to the charging of electric vehicles.

This way it is possible to fully understand the choices made later during the study of the charging system consisting of a Voltage source inverter (later VSI) and a synchronous permanent magnet motor (later PMSM) for automotive applications.

1.2.1 Charging Columns and Connectors

The recharging column for electric vehicles, better defined as Electric Vehicle Supply Equipment (later EVSE), is the electricity distributor through which an electric vehicle can be recharged.

Two categories of EVSE can be identified:

- **Private or Semi-Public:** usually pre-wired and connected to the customer's counter, usually installed by a technician. The fields of employment are shopping centers, shops, restaurants, hotels, car showrooms with workshops, banks etc.
- **Public:** onstalled by energy suppliers on public roads, public parkings etc.

By 2030, more than the 90% of the EVSE will be private [4], while over the 80% of EV charging is currently taking place at home. [5]

To identify the four modes currently permitted for vehicle charging it is made reference to **CEI EN 61851-1** [6]:

	Characteristics
Mode 1	Slow charge in domestic environment
Mode 2	Slow charge in domestic environment, with Control Box
Mode 3	Slow or moderately rapid charge in domestic or public environment
Mode 4	Average or ultra fast recharge in public environment

Table 1.1: Charging modes definitions

1.1 shows the four charging modes, but it is useful to make more distinctions between them.

Mode 1

It takes 6 – 8hr to completely recharge the battery, with a maximum current of 16A. It is possible to use both an industrial socket or a household one (Schuko). This mode is not usually used for automotive applications.



Figure 1.2: Charging Mode 1

Mode 2

The charging time is again 6 – 8hr, but with a maximum current of 32A and a higher level of security guaranteed by a *Control Box*, also defined *In-cable Control and Protection Device* which ensures safe operation during charging with a basic PWM circuit. However this mode is only allowed in private environment.

It is possible to use both domestic and industrial sockets (both single-phase and three-phase) up to 22kW power. It can be seen like a portable CA charging station to use when no fixed station is available.



Figure 1.3: Charging Mode 2

Mode 3

The charging time can be slow as in Mode 1 and Mode 2 or moderately rapid, that means a charging time between 30min and 1hr.

For slow recharge the maximum current is 16A, while for average charge one is up to 70A for single-phase 250V maximum voltage or 763A for three-phase 500V maximum voltage. Fixed stations, columns or wall boxes specific for charging electric vehicles which incorporate PWM control and protection functions. Power up to 22kW.

This mode is mandatory in public environments and it needs specific connectors regulated by CEI EN 62196-1 [7] and 2 [8]. Three possible types of connectors

are available: [9]

	Maximum power	Voltage	Current	Plug Contacts
Type 1 SAE SAE J1772	19 kW	1-phase 230V	32A	5
Type 2 Mennekes VDE-AR-E 2623-2-2	22 kW	1-phase 250V 3-phase 500V	1-ph 70A 3-ph 63A	7
Type 3 EV Plug Alliance 3A	4 kW	1-phase 250V	16A	4
Type 3 EV Plug Alliance 3C	22 kW	1-phase 250V 3-phase 500V	1-ph 32A 3-ph 63A	7

Table 1.2: Charging types Mode 3



Figure 1.4: Charging Mode 3

Mode 4

The charging time goes from $1hr$ to $10min$, this charging mode is allowed only in public environments and it provides a direct current up to $400A$ with up to $350kW$ power. This mode is regulated by the **CEI EN 61851-23 [10] and 24 [11]** standards and needs CCS Combo (**CEI EN 62196-3 [12]**) or CHAdeMO connectors.

- **Type 4 - CHAdeMO**

The plug counts 10 contacts: 2 for the DC line, 1 for the ground and 7 for control. The maximum voltage is $500V$ while the maximum current is $80A$ for average fast charge and $200A$ for ultra fast charge.

- **Combo1 - Universal connector (CCS1)**

It is an evolution of SAE J1772, with in addition 2 contacts for the DC line. Moreover, it is possible to set up a three-phase charge by using the 2 contacts dedicated to the DC line.

It is possible to connect the SAE J1772 to the universal Combo1 socket.

- **Combo2 - Combined Charging System (CCS2)**

Proposed by Mennekes in the wake of Combo1 by SAE. Same principle of Combo1 but not widely distributed yet.



Figure 1.5: Charging Mode 4

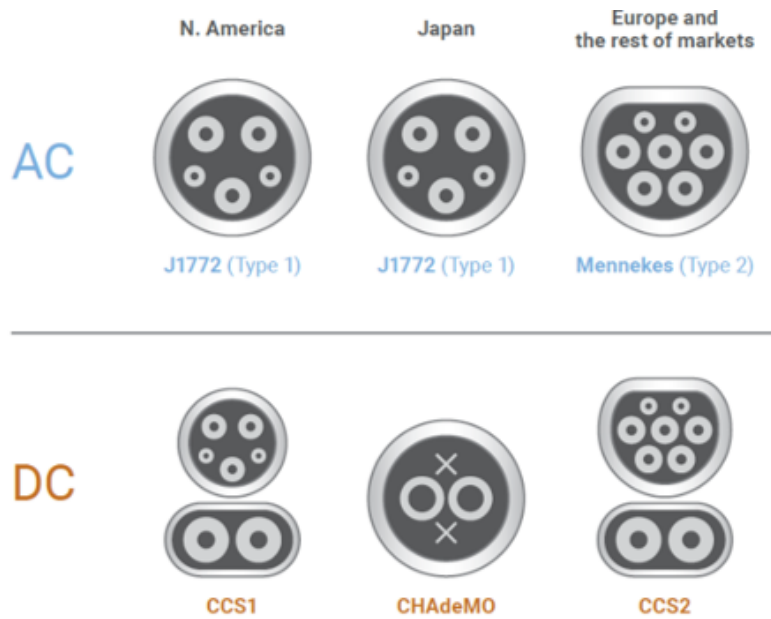


Figure 1.6: Connectors types

1.2.2 Current International Situation

USA

Few use of charging mode 1 (poor diffusion of grounding), mode 2 is the most diffused. Mostly used SAE J1772 and Combo1 in public.

Japan

CHAdeMO widely spread and also allowed in private. Also SAE J1772 is diffused. Combo1 begins to spread now.

Europe

CHAdeMO in a good number of recharging points, while SAE J1772 and Combo1 are not very common. Mennekes connectors are widely spread in Germany, but France seems to prefer Type 3. At the beginning of 2013 the Commission chose the Mennekes connector as a single standard.

Italy

CHAdeMO charging points are very few. **CEI EN 61851-1:2012 paragraph 11.3.2** standard imposes the use of screens or other safety systems. This banned the use of Mennekes connectors in Italy, which however became the only standard. In order not to lose the market share given by the Italian people, Mennekes began to produce connectors with shutters, to cover Italian market. Both Mennekes and Type 3 are now widespread.

1.2.3 Power Cables

CEI 20- 106 published in 2013 imposes standards while waiting for a European legislation. This standard regulates the manufacture of cables used for charging vehicles. It provides an ambient temperature between $-30^{\circ}C$ and $+50^{\circ}C$, the maximum permanent service temperature of the conductor is set at $90^{\circ}C$.

The maximum voltage is $450/750V$.

1.2.4 Conclusions on Charging Modes and Connectors

It is simple to understand that the desired charging mode for this application could be mode 3. Basically because charging modes 1 and 2 do not fit for this type of application as they are not dedicated for automotive applications. On the other side, mode 4 provides for DC charging.

For mode 3 four types of connectors are provided, but type 3A is not dedicated for automotive applications. Type 1 (SAE J1772) must be discarded because it is only useful in case of single-phase charging, while type 2 and type 3C have similar characteristics.

However, considering actual European and Italian standards, Mennekes VDE-AR-E 2623-2-2 seems to be the forced choice. It will be possible to use a maximum current of $63A$ with a maximum three-phase line voltage of $500V$, with a maximum power limited to $22kW$.

1.3 Parasitic Currents Standards

The presence of parasitic currents in the motor housing could lead to critical safety issues. Unfortunately there are not dedicated standards setting the maximum accepted current circulating in the motor housing, so it is reasonable to consider the maximum current that does not affect the human health.

Again, it is not a simple matter: the maximum current considered safe for humans depends on the duration of exposure and the path the current takes through the body. The effects of electrical currents on the human body are well-documented in standards and research, with particular emphasis on thresholds for safety. Here are some key points:

- **Threshold of Perception:** The minimum current at which a person can feel the sensation of electric shock is typically around 1 mA (milliampere) for alternating current (AC) and 5 mA for direct current (DC) [13].
- **Let-Go Threshold:** This is the maximum current at which a person can voluntarily let go of an electrically live object. For an average adult, this threshold is approximately 10 mA for AC and 60 mA for DC [13].
- **Threshold of Ventricular Fibrillation:** The most dangerous effect of electric shock is ventricular fibrillation, which can be fatal. The threshold for causing ventricular fibrillation is around 30 mA for AC currents and 300 mA for DC currents, assuming the current passes through the chest area [14].
- **Safe Exposure Limits:** According to IEC 60479-1, "Effects of Current on Human Beings and Livestock," the following currents are considered dangerous:
 - For AC (50-60 Hz): Currents above 30 mA can cause severe shock and possible respiratory paralysis. Currents above 100 mA can cause ventricular fibrillation.
 - For DC: Currents above 300 mA can cause ventricular fibrillation.
- **Regulatory Standards:** The Occupational Safety and Health Administration (OSHA) and other regulatory bodies often reference these thresholds in safety guidelines and standards.

European Standards for Electric Motor Currents

The European standards and regulations related to the currents that can flow in an electric motor housing primarily focus on safety, efficiency, and operational integrity. However, while specific maximum current values are not detailed in the general standards, the regulations ensure that motors are designed to handle the electrical stresses safely. These include the ATEX directive for explosive atmospheres, ecodesign regulations for efficiency, and specific research on managing internal currents to prevent damage and ensure longevity of the motor systems.

Ecodesign Regulation (EU) 2019/1781

The Ecodesign Regulation (EU) 2019/1781 sets energy efficiency requirements for electric motors and variable speed drives (VSDs) across a wide range of power ratings. While it primarily addresses efficiency levels (IE2 to IE4 depending on motor characteristics), it also includes requirements for performance and safety under different operational conditions. However, it does not explicitly specify maximum allowable currents within the motor housing, focusing instead on the overall efficiency and operational parameters of the motor [15].

ATEX Directive (94/9/EC)

The ATEX directive is crucial for motors operating in potentially explosive environments. It requires that motors used in such environments meet stringent safety standards to

prevent ignition from electrical discharges. This includes ensuring that the motor housing can handle electrical currents without causing sparks or overheating, which could ignite combustible materials in the environment. This directive is applicable to industries dealing with combustible dusts and gases, ensuring that motors are designed to safely manage the electrical currents flowing through them [16].

Common-Mode Voltage and Bearing Currents

Research has shown that the common-mode voltage and bearing currents in motors, particularly those driven by silicon carbide (SiC) inverters, need careful management. High switching frequencies and voltages can lead to increased discharge energy, which can cause electric corrosion in the motor bearings. Methods to mitigate these effects include designing common-mode filters and adopting specific pulse width modulation strategies to reduce bearing voltage and currents, thereby protecting the motor housing and internal components from excessive electrical stress [17].

1.4 Motor Structure

As anticipated, the electric machine in study is a multi-phase motor, in particular it is a nine-phase one.

Multi-phase machines are gaining more and more fame in traction applications because of their high reliability, fault tolerant capability, as well as the low weight and volume. Last but not least, they offer a very high efficiency [18].

To be more specific, multi-three-phase machines are an interesting subset of multi-phase machines. The benefits that derive from this type of electric motors can be easily resumed in a very low current ripple and a high fault tolerance because of the autonomous operation of the stars. To obtain a battery charger by using this particular type of machine, the possibility of access to the three star centers of the windings makes the nine-phase machine a perfect candidate. In fact, a three-phase voltage source could be connected to the star centers to recharge the battery, but this will be described in next subsection.

The electric motor used for the development of this thesis is a prototype realized inside PEIC laboratories of Politecnico di Torino. It is a symmetric PMSM with concentrated winding and surface mounted magnets. The concentrated winding stator benefits are the simple construction with a reduction of frontal connections and the related losses reduction.

The first draft of the motor was already available, but a new version with in-cave cooling system called Cool-X was assembled during the development of this thesis. Main motor data are listed in next page.

External diameter	142 mm
Internal diameter	79.66 mm
Airgap	0.5 mm
Active length	101 mm
Number of teeth	9
Number of magnets	10
Tooth height	15.8 mm
Tooth width	14.2 mm
Cave width	25.1 mm

Table 1.3: Motor data

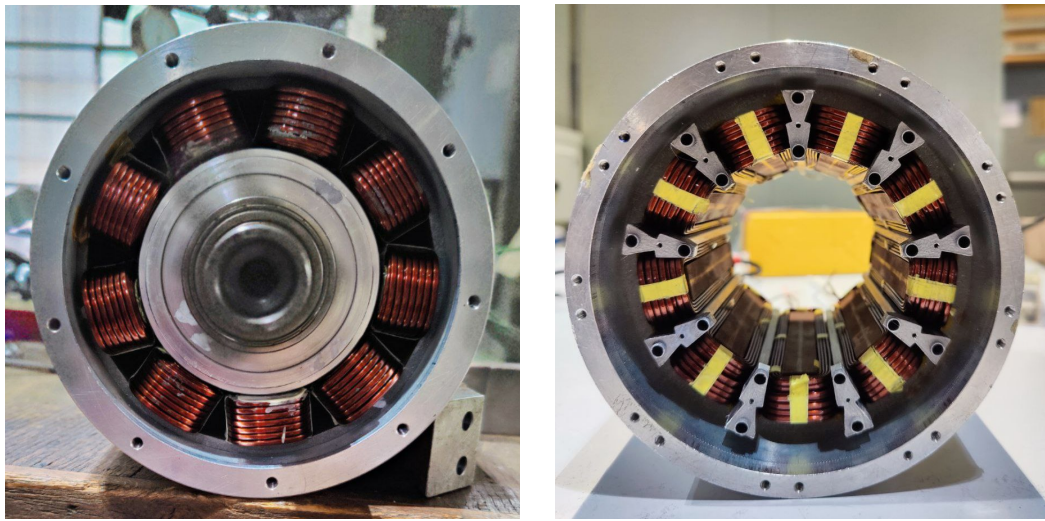


Figure 1.7: First draft and final prototype motor section

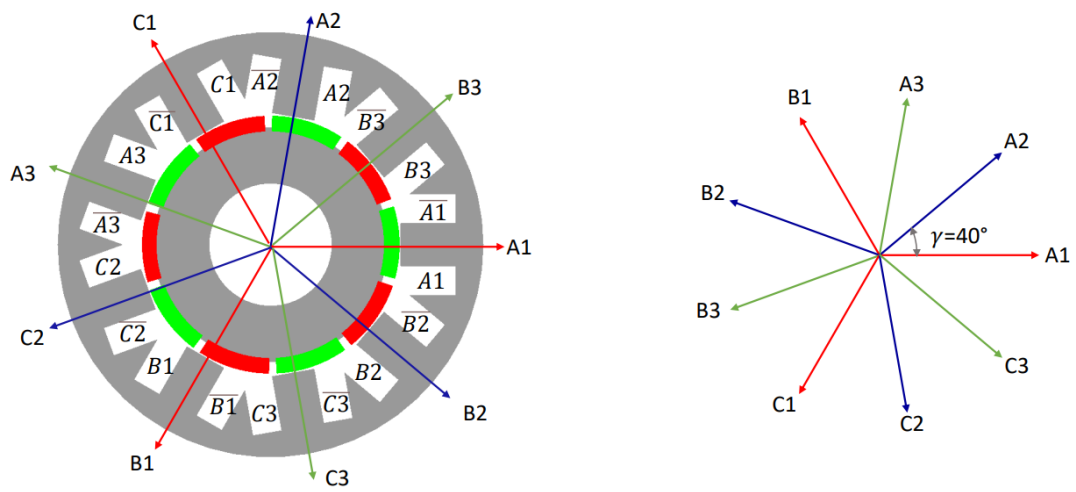
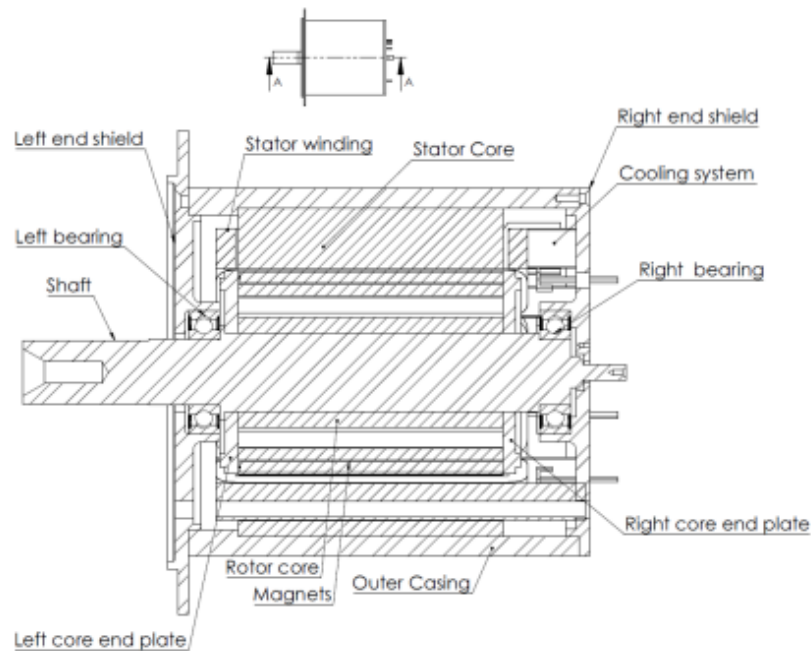


Figure 1.8: Phase displacement between the terms**Figure 1.9:** Motor components

1.5 Integrated On-Board Battery Charger

As written above, it is possible to find charging columns for electric vehicles that offer both direct and alternating current, both mono- and three-phase. However, it is known that the grid only provides AC and, therefore, a conversion stage is needed to get the DC charging. Of course, even "charging the vehicle" using AC will require an AC/DC conversion stage somewhere before reaching the battery. This is the point where on-board and off-board chargers differ.

DC off-board chargers, also referred as standalone chargers, represent an ideal solution to shorten the charging time of electric vehicles. The conversion stage takes place inside the charging column, that means outside the vehicle. It allows to take advantage of much higher charging powers than the AC charging columns, which results in very short charging times.

However, it is not possible to find a DC charging column everywhere, while it is easier to directly exploit the AC network, for this reason the majority of current electric vehicles is equipped with on-board chargers.

On-board chargers bring the AC/DC conversion stage inside the vehicle, making charging points more accessible but losing the advantage of ultra-fast charging.

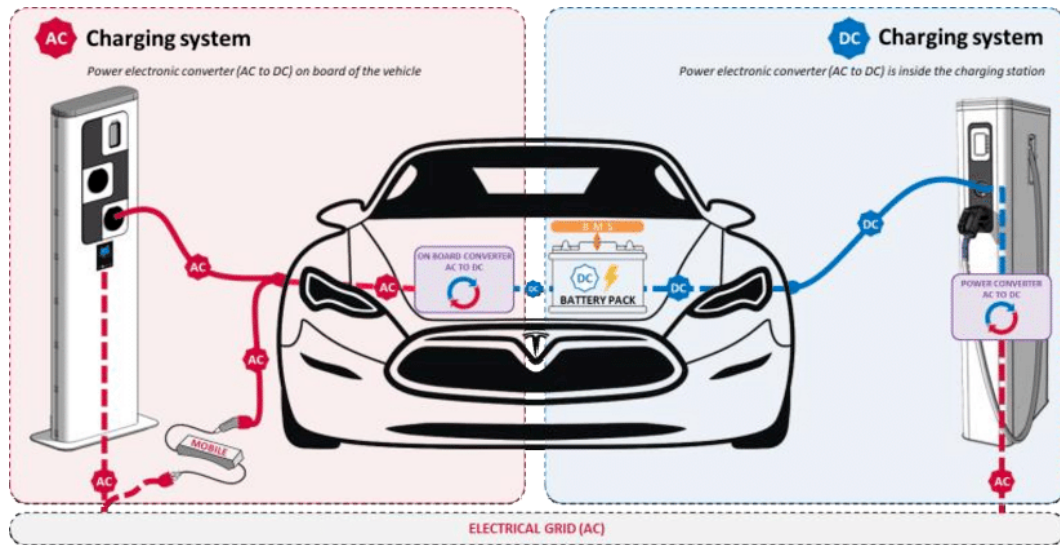


Figure 1.10: On-board vs off-board chargers

One of the aims of this research is to obtain the advantages of both DC and AC charging, combining in one integrated on-board charger both the solutions. It will be able to combine not only the mono- and three-phase charging, but also the DC one. The configuration will scarcely change for the two cases but the purpose of using only components already present inside the vehicle will be respected.

Going into detail about the components involved, a simple schematics follows to better understand the system usage.

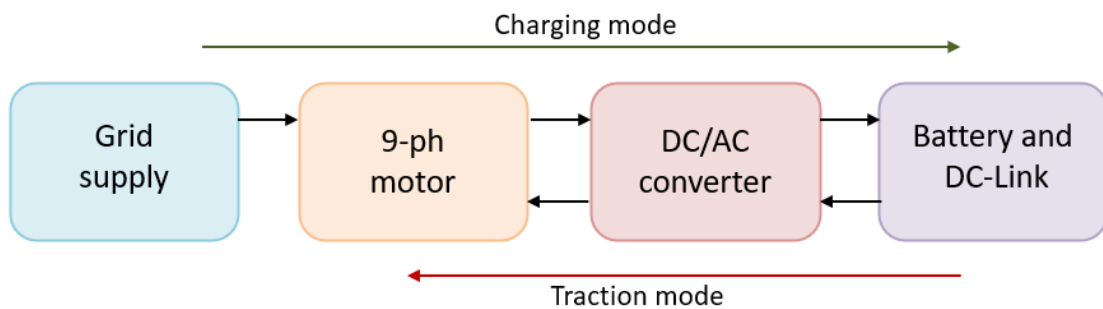


Figure 1.11: Simple system scheme

Obviously, 1.11 excludes the block named "grid supply" in traction mode because the vehicle would not be connected to the grid when it moves. However, the possibility of using the vehicle battery as a generator in special cases and with the necessary protocols is not excluded.

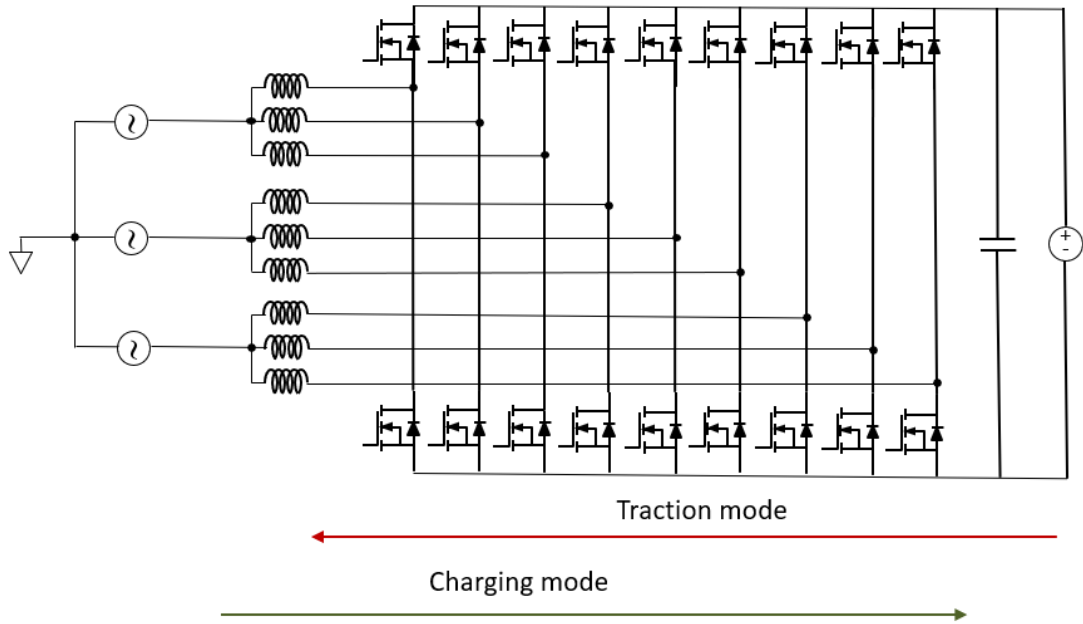


Figure 1.12: Electrical scheme

Figures 1.11 and 1.12 show the components used for traction and recharge mode, with the battery feeding the nine-phase VSI itself connected to the electric motor during traction mode. To recharge mode, instead, also grid supply is considered, with the electric motor acting basically like nine inductors and VSI working like a diode rectifier. In fact, considering the winding like simple inductors and using the MOSFETs diodes, the systems would be similar to a diode rectifier with DC-DC boost converter.

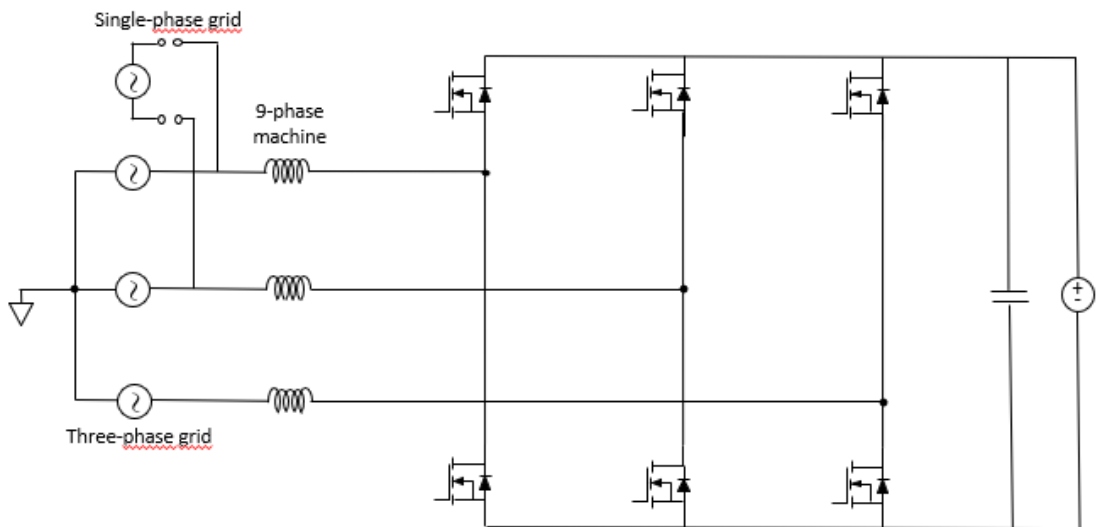


Figure 1.13: Equivalent charging scheme

1.5.1 Grid Supply

Standards [19] and [20] provide standards about grid nominal voltage and acceptable overvoltages.

Focusing on the nominal voltage of low voltage grids, the $\pm 10\%$ tolerance to the nominal value brings to further considerations resumed in 1.4

Nominal V_{rms}	V_{rms} max & min	V_{pk} max & min
$400 V_{rms} \pm 10\%$	$440 V_{rms}$	$622 V_{pk}$
	$360 V_{rms}$	$509 V_{pk}$

Table 1.4: Peak and rms maximum and minimum voltage values

Table 1.4 evidences that, even if the rated value of the three-phase line-to-line voltage is $400V$, up to $622V_{pk}$ is considered within the range of acceptable voltage values.

Moreover, standard [19] provides for the consideration of a series of overvoltages that may occur within the electricity network. In particular, these overvoltages are divided between $110\% V_n \leq V \leq 120\% V_n$ and $V \geq 120\% V_n$.

Reasonably, at the design stage it is chosen to consider overvoltage values only up to $130\% V_n$, that means $520 V_{rms}$ and $735 V_{pk}$.

In conclusion, the maximum acceptable grid peak voltage value has been established to $735 V$. This means that the required switches for the power converter will have to withstand a rated voltage reasonably greater than this value.

In addition, it will need a battery voltage much greater than $735 V$, to exclude the possibility of an undesired current running from the grid to the battery.

1.5.2 Battery Specifics

As already written above, the main problem with the choice of battery voltage is the risk of having an undesired current running from the grid to the battery. This would be possible, for example, in vehicle-to-grid operation. In this case, there are no components to break the current as shown in figure 1.14.

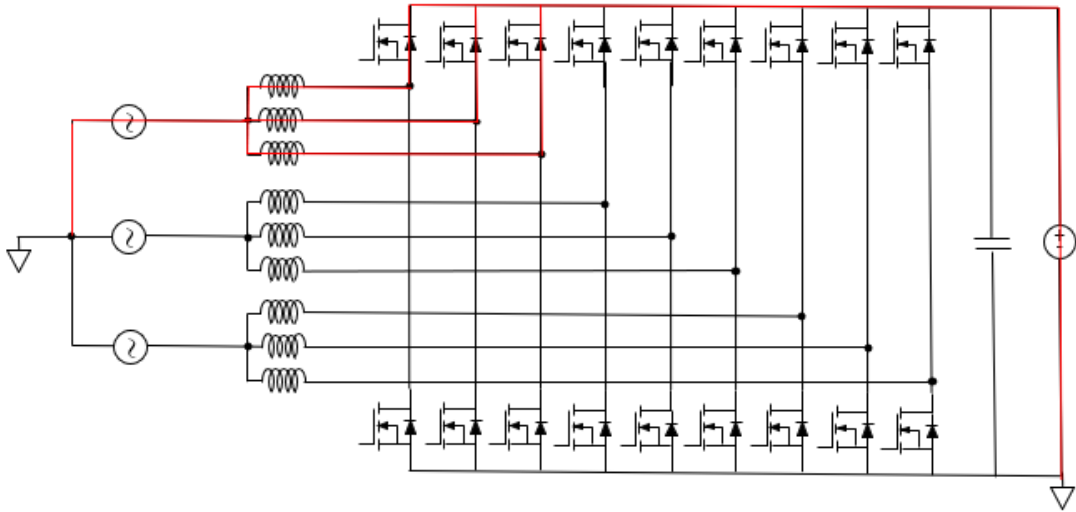


Figure 1.14: Grid-to-battery undesired current

That is why the choice of the battery must fall on one with a minimum operative voltage higher than the maximum peak voltage coming from the grid.

Having a maximum grid peak voltage of 735 V it has been chosen to consider at least a 1000V nominal voltage battery.

It is not sufficient to know just the nominal voltage of the battery: in fact, it must be considered minimum and maximum operative voltages and keep the minimum one over 735 V .

Maximum and minimum operative voltages of the battery depend on maximum and minimum operative voltages of the cells. For this automotive application, it has been chosen to consider lithium nickel manganese cobalt oxide (LiNiMnCoO_2 , later called NMC) cells instead of lithium-ion or lithium iron phosphate (later called LiFePo_4) ones. The reason behind this choice is the higher energy density and capacity of NMC cells with respect to LFP ones, meaning less series-parallel links and space save. Moreover, the nominal, maximum and minimum voltage of NMC cells are higher than the ones of LFP cells.

However, NMC cells lifecycle is less than the one of LFP cells and the cost is higher.

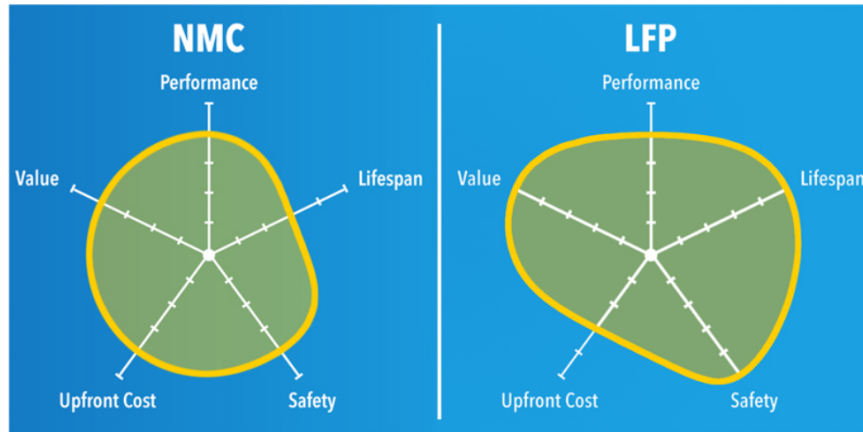


Figure 1.15: LFP vs NMC cells

The overall performance of LFP and NMC batteries is almost the same. The choice of NMC cells was dictated by the need to have a high energy density and a higher cell voltage. Table 1.5 summarizes main differences between the two types of cells [21].

Parameter	LFP	NMC
Nominal voltage	3,3 V	3,6 V
Maximum voltage	3,7 V	4,2 V
Minimum voltage	2,5 V	3,0 V
Capacity	90 – 120 Wh/kg	150 – 220 Wh/kg
Cycle life	≥ 2000 cycles	1000 – 2000 cycles
Cost	\$200 per kWh	\$420 per kWh

Table 1.5: LFP and NMC cells comparison

Having a nominal voltage of 1000 V with NMC cells means having a maximum operative voltage of 1170 V and a minimum voltage of 833 V, sufficient for the requirements about grid voltage.

To stay in line with current research it has been decided to choose a 1200 V battery, with maximum voltage equal to 1400 V and minimum voltage equal to 1000 V. It would not be possible to further increase the voltage of the battery because of low voltage standards that limit DC voltage to a maximum value of 1500 V [22]. Exceeding this voltage would mean passing in medium voltage and the insulation standards would be inapplicable for automotive purposes.

1.5.3 Switches Selection

As a maximum battery voltage of 1400 V has been considered, switches choice must fall on reasonably higher rated voltages.

In traction mode the switching frequency is supposed to be around 20 kHz, this means it is necessary to use special devices as Silicon Carbide MOSFETs (later called SiC) or Gallium Nitride transistors (later called GaN).

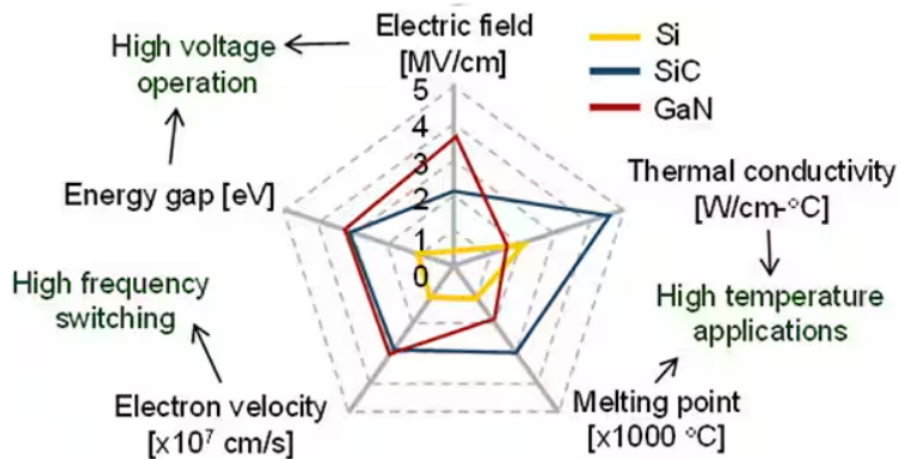


Figure 1.16: Si, SiC and GaN devices comparison

Wide bandgap materials like silicon carbide and gallium nitride have wider energy gaps than "normal" silicon devices (approximately three times more) and very higher breakdown electrical fields. This last property is about ten times with respect to silicon devices and permits a better utilization of the device at high voltages.

Moreover, these devices offer higher blocking voltage and lower on-state resistance that bring to lower conduction losses and approximately no reverse recovery which allows to obtain lower switching losses. To have lower losses permits a higher frequency utilization of the device.

A negative aspect of wide bandgap devices is the strong temperature dependency of the on-state resistance.

Figure 1.16 shows main characteristics and related applications for Si, SiC and GaN devices. It is evident how SiC and GaN devices are more suitable for the studied application.

Due to the better thermal characteristics and commercial availability, the choice fell on SiC devices.

Wolfspeed[23] is one of the main SiC MOSFETs provider, 1700 V rated SiC MOSFETs are available on the website.

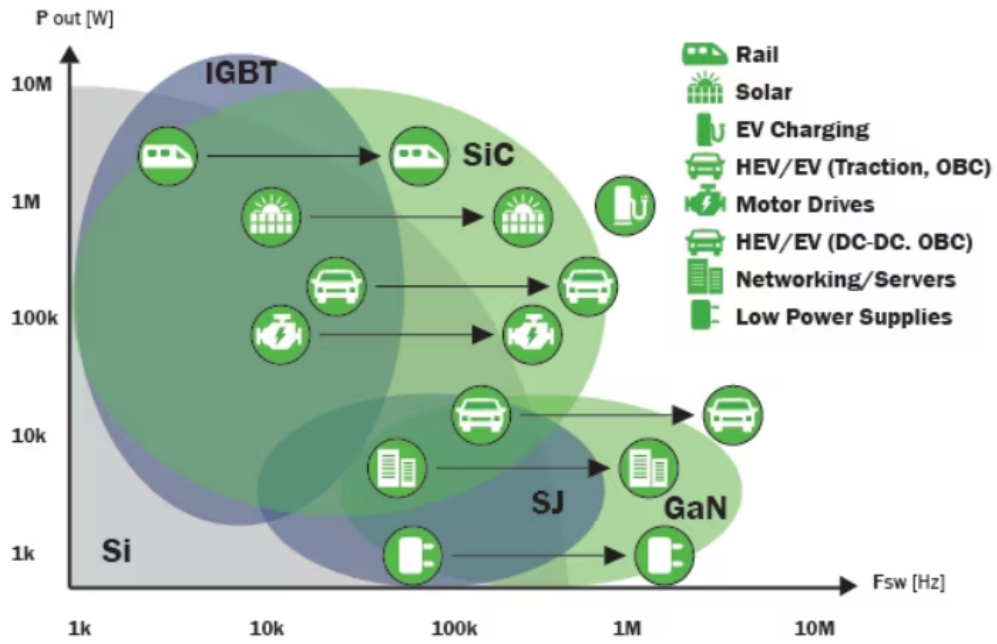


Figure 1.17: Power capability versus switching frequency for popular high-voltage, high-current transistors and other devices, as well as primary applications

Chapter 2

Preliminary Verification of the Presence of Null Torque during Charging

The primary concern when developing an integrated battery charger for multiphase electric motors is the potential generation of electromagnetic torque in the rotor during the charging phase. If electromagnetic torque is generated, it could lead to undesirable vibrations within the motor or, in the worst-case scenario, cause the vehicle to move while charging. Addressing this issue is crucial for ensuring the safety and reliability of the charging process.

Electrotechnics theory provides a foundational understanding of how torque generation can be managed in such systems. According to this theory, the average torque generated by each set of windings can be nullified by injecting current into the accessible star center of each winding set. This principle is well-supported by existing literature, which confirms that it is possible to achieve an average null torque value through appropriate current injection strategies. Essentially, by carefully controlling the current input, the overall electromagnetic forces can be balanced in such a way that the net torque over a cycle averages to zero.

Paper [24] explore this principle in depth. They demonstrate that it is feasible to design systems where the average electromagnetic torque is zero during charging. However, they also emphasize the necessity of ensuring that the instantaneous torque does not cause rotor movement, highlighting the complexity of real-world applications. However, ensuring that the average torque is zero is not sufficient to guarantee that the rotor will remain stationary during the charging phase. This is because even if the average torque over time is zero, there could still be instantaneous variations in torque that could cause the rotor to move. It is crucial to ensure that the instantaneous (or punctual) torque is zero to prevent any unwanted rotor motion. Instantaneous torque can arise from transient current imbalances or harmonics in the electrical system, which might not

be evident when only considering average values.

If there is any instantaneous torque generated, it could necessitate the use of a mechanical lock to prevent rotor movement during charging. This, however, introduces additional challenges. Mechanical locks can create mechanical stress within the motor and its associated components, potentially leading to wear and tear or even damage over time. The mechanical stress induced by such locks can compromise the integrity and longevity of the electrical machine, necessitating more frequent maintenance or leading to unexpected failures.

Paper [25] further investigates these challenges. They discuss advanced methods to control current waveforms to minimize instantaneous torque fluctuations in multiphase systems. Their findings underscore the importance of sophisticated control strategies to manage both average and instantaneous torque effectively.

Therefore, the design of an integrated battery charger must carefully consider the patterns of current injection and their impact on instantaneous torque generation. This involves a detailed analysis of the current waveforms and the electromagnetic interactions within the motor. Advanced control strategies, such as field-oriented control (FOC) or direct torque control (DTC), can be employed to finely tune the current inputs and minimize instantaneous torque fluctuations. Additionally, the use of sophisticated modeling and simulation tools can aid in predicting and mitigating torque-related issues during the design phase.

By achieving a zero instantaneous torque, the system can avoid the need for mechanical locks and the associated mechanical stresses, ensuring a safer and more reliable charging process. This requires a holistic approach that encompasses both theoretical understanding and practical implementation, integrating advanced control techniques with rigorous testing and validation.

The first question arising during the study of the integrated battery charger is if it would be possible to effectively generate no electromagnetic torque in the rotor during the charging phase. Otherwise, it would generate vibrations inside the motor or even worse the vehicle could move while charging the battery.

Following electrotechnics theory, the average torque generated by each of the three terns of windings would be null by injecting current into the accessible star center of each of them. Bibliography confirms the presence of an average null torque value [24] [25].

However, it is not sufficient to know that the average torque value would be null to make sure that the rotor would not start rotating during the charging phase. It is necessary to ensure that the punctual torque generated is zero, otherwise it would be needed to insert a mechanical lock during the charging phase, running the risk of generating mechanical stress inside the electrical machine.

2.1 FEM 2D Simulations

2.1.1 Introduction to Finite Element Analysis (FEA) and Finite Element Method (FEM)

Finite element analysis (FEA) is the process of simulating the behaviour of a part or assembly under given conditions so that it can be assessed using the finite element method (FEM) in order to reduce the need of physical prototypes to test.

The simulations used in FEA are created using a mesh of millions of smaller elements that combine to create the shape of the desired structure. Each of these small elements is subjected to calculations, with these mesh refinements combining to produce the final result of the whole structure. These approximate calculations are usually polynomial, with interpolations occurring across the small elements, meaning that values can be determined at some but not all points. The points where the values can be determined are called nodal points and can usually be found at the boundary of the element.

2.1.2 2D Motor Simulation

To verify the presence of average null torque a Finite Element Method (later called FEM) simulation of the motor has been created, as it would be too difficult to analytically perform the calculations.

The software used for the simulation is FEMM 4.2 [26], a 2D specific tool for electrostatics and magnetics simulations.

FEMM 4.2 requires the peak values of the currents as parameters. For the first simulation they were chosen equal to 500 A for 1 turn and belonging to a symmetrical tern, as grid supply ones.

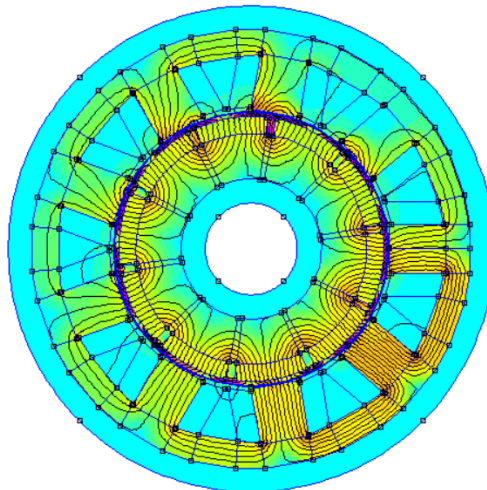


Figure 2.1: FEMM 4.2 simulation plot

Since FEMM 4.2 only allows to analyze static cases, the simulation has been performed choosing a precise point represented in the figure 2.2, with one of the three sinusoids that assumes the peak value.

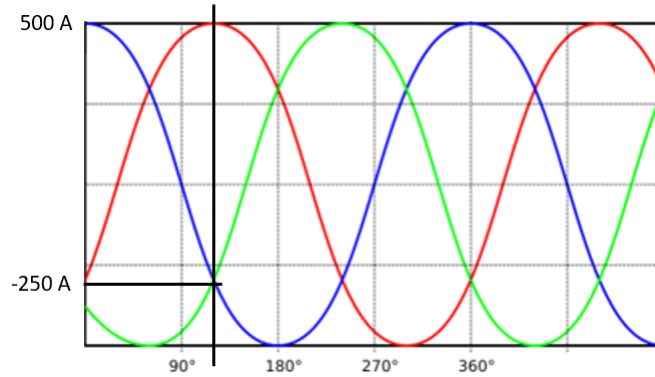


Figure 2.2: Grid 3-phase supply

A series of simulations were launched considering the same current and different rotor positions (width of the ranges: 5°). Results are shown below with a torque maximum absolute value of $2,45Nm$.

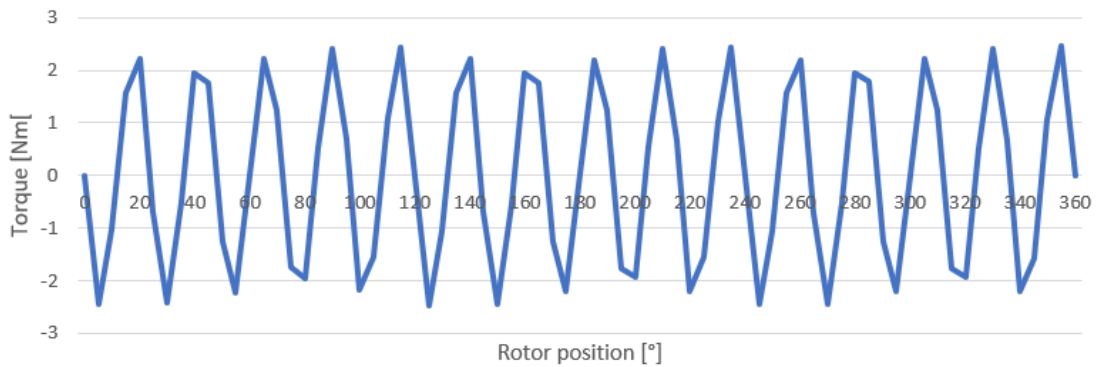


Figure 2.3: Torque generated for different rotor positions

From the simulation plot it is clear that the average generated torque is zero, with positive and negative torque peaks depending on the rotor position. Two other plots were produced considering the peak of the other two currents of the tern and obviously finding the same trend.

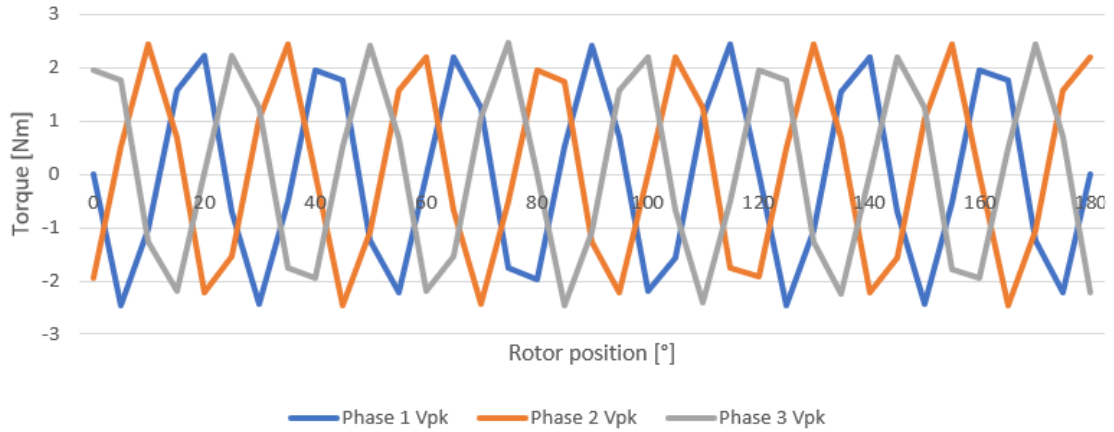


Figure 2.4: Three-case comparison

The results of these first simulations make evident the presence of a torque with zero average value, as expected. It is not yet clear whether this torque can give a movement to the rotor.

Next step is to simulate a time variation of the current by considering different "points" on the current sinusoids. Figure 2.5 shows on phase 1 the considered cases.

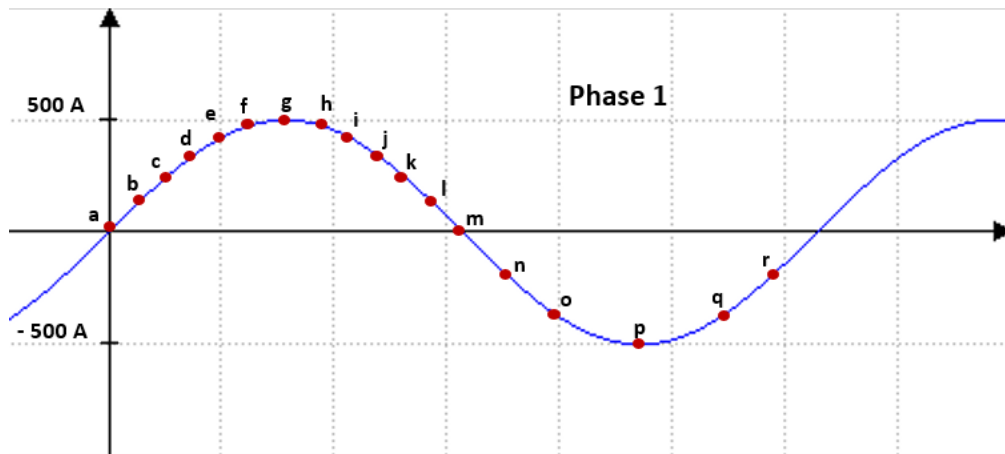


Figure 2.5: Considered points of phase 1 current

Clockwise and counterclockwise rotations of the rotor have been examined to validate the simulation.

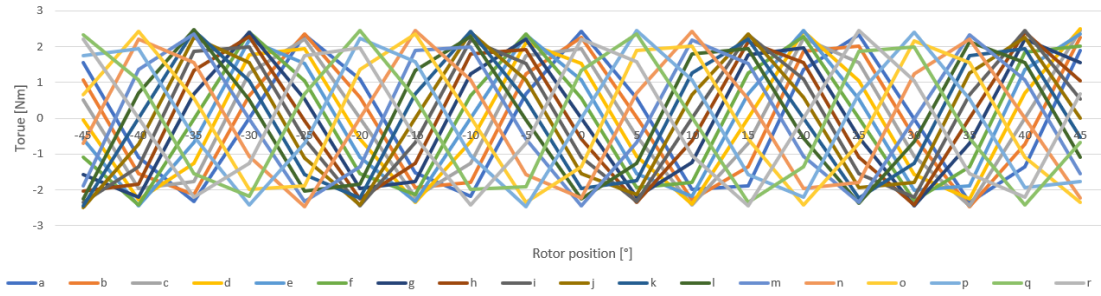


Figure 2.6: Torque generated for different moments and rotor positions



Figure 2.7: Detail of the torque generated for different moments and rotor positions

It is evident an identical trend with respect to the first simulations, with an appropriate offset between the cases.

FEM simulation results open to the possibility of having an average non-null torque in the motor. It is not yet clear if it would be a ripple or not.

2.2 MATLAB Script to identify Synchronous Harmonics

It is known that in a brushless motor the torque can be calculated as:[27]

$$T = \frac{3}{2}P[i_q\Lambda_0 + (L_d - L_q)i_d i_q] \quad (2.1)$$

2.1 equation evidences the presence of two contributors: the first one is due to the interaction between the magnetic field produced by the permanent magnets and the one produced by the stator windings, while the second term indicates the reluctance torque generated by the interaction between the stator field and the rotor anisotropy. The second contribute is clearly null for a PMSM.

In the ideal case of having just the fundamental component of the two magnetic fields, this interaction produces a constant torque term. Vice versa, if harmonic content is

present in the distributions, then there is also an oscillating term.

It also must consider the cogging torque due to the interaction between the magnetic field produced by the magnets and statorical teeth.

In particular, for the studied case there is not a fundamental component, but it is necessary to know if the same harmonics are present in the two distributions and, so, if a synchronous torque would be produced.

MATLAB script is available in appendix A. It performs the convolution product between permanent magnets induction distribution and stator windings distribution to plot the synchronous harmonics that could generate an oscillating torque.

In figure 2.8 is clearly present the 15th harmonic. 6th and 45th ones can also be identified. Figure 2.9 offers a bigger detail of the harmonics, even those with negligible amplitudes.

Having a number of five pole pairs, multiple harmonics of the number of pole pairs contribute to torque generation. It is clear the very low contribute of the fifth harmonic and the absence of tenth one. Higher order harmonics are neglected. A null torque is expected from the experimental test.

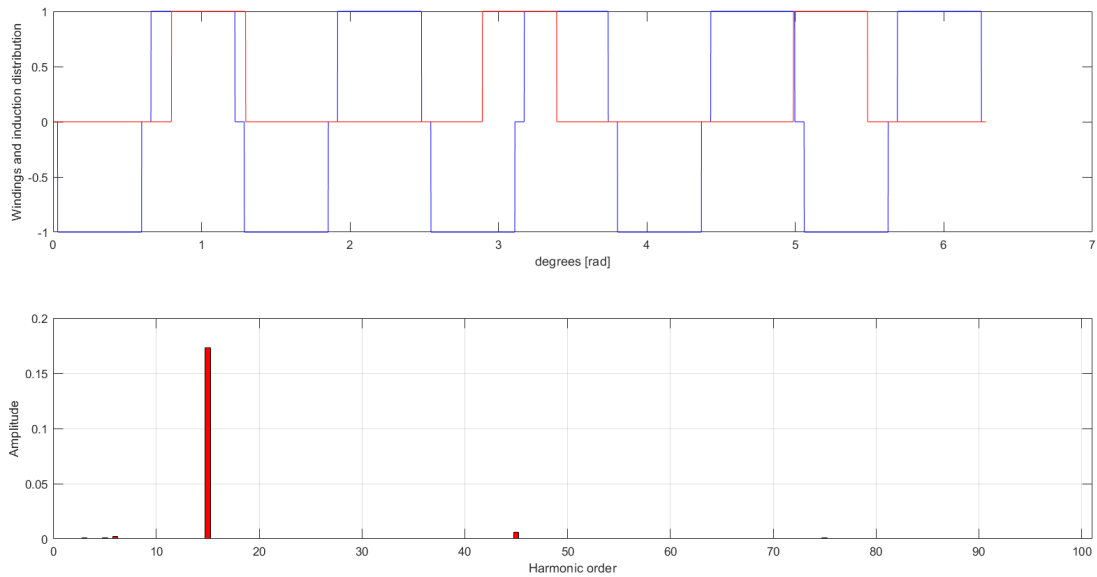


Figure 2.8: MATLAB plot showing distributions and synchronous harmonics

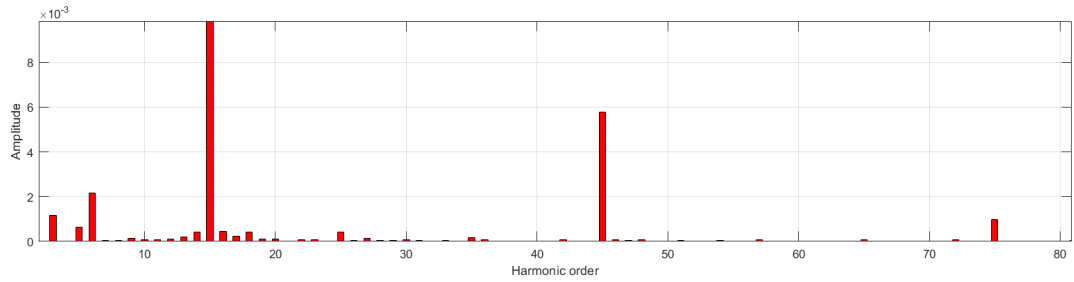


Figure 2.9: MATLAB plot detail of low amplitude synchronous harmonics

2.3 Experimental Setup and Results

To validate the simulation results, experimental tests were carried out and the obtained results are presented in this section.

First, insulation and continuity tests were performed on the motor to verify the absence of short-circuits. It has been verified the insulation between the three star centers and between star centers and motor housing (Fig. 2.10)

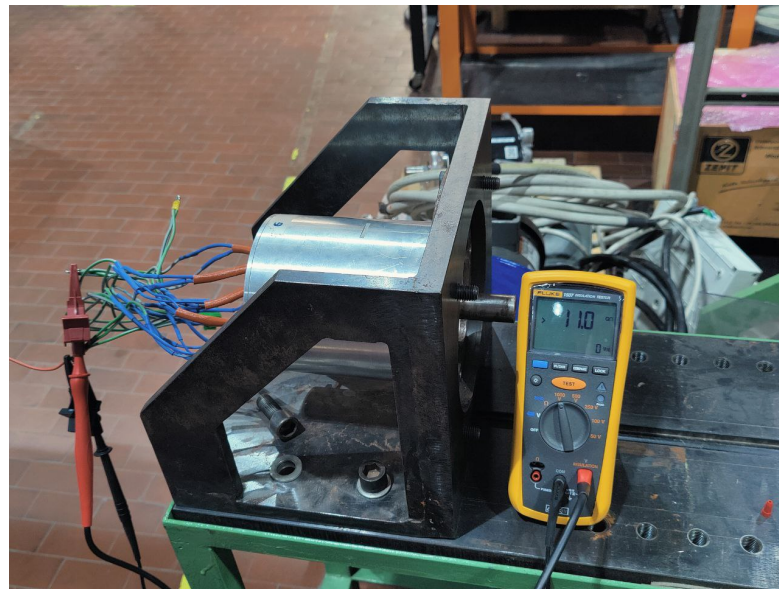


Figure 2.10: Phase-to-phase insulation test

Once verified the insulation of the machine, the three star centers have been fed at the grid frequency by using an autotransformer to simulate the grid as shown in figure 2.12.

An autotransformer is an electrical transformer with only one winding (per phase). In an autotransformer, portions of the same winding act as both the primary winding and

secondary winding sides of the transformer. They are frequently used as an economical alternative to three phase general purpose distribution transformers to adjust the supply voltage to match specific load requirements when load isolation from the supply line is not required.

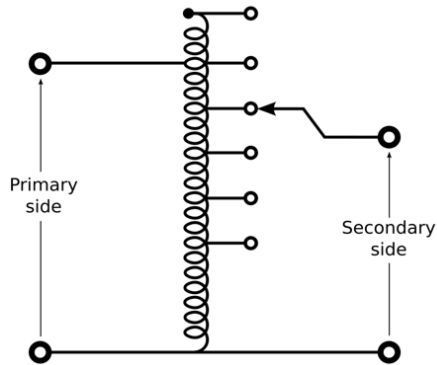


Figure 2.11: Autotransformer scheme



Figure 2.12: Autotransformer that reproduces the grid

It is not sufficient to connect the auto-transformer to the motor. In fact, current must flow to generate the torque as indicated in equation 2.1. To do this, a diode rectifier and a resistive load have been introduced. In particular, the aim of the test was to feed the motor with a sinusoidal current to simulate the grid. To do this, three three-phase full wave diode rectifiers as the one shown in figure 2.13 have been used, one for each tern of

phases.

The current absorbed by the diode rectifier, when using a resistive load, can be approximated to a sinusoidal wave considering the filtering effect of the inductance of the windings as indicated in figure 2.14.

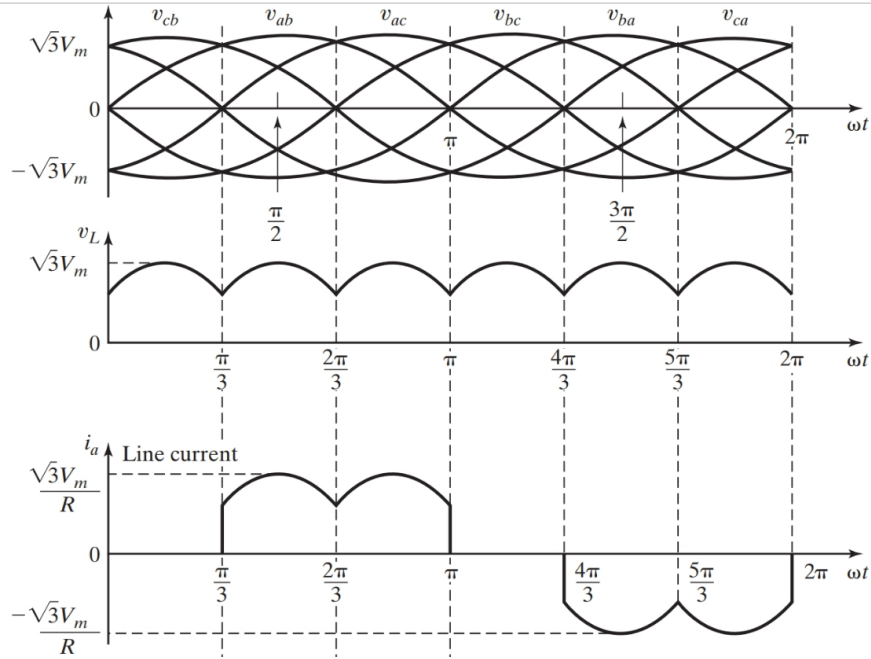


Figure 2.13: Full wave three-phase rectifier waveforms

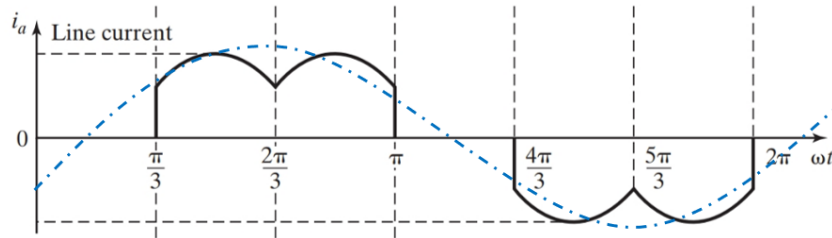


Figure 2.14: Filtered line current

To complete the circuit, a bench of high dissipation resistors (figure 12.15) was used. Each resistor has a 54Ω resistance, two resistors in series were used to carry out the test. Experimental setup is shown in figure 2.18 and in scheme 2.16.

A current clamp and a voltage tester were connected on the DC side of the circuit to measure the current absorbed by the load and the output voltage of the rectifier. Measurements are listed below.

V_{dc} [V]	I_{dc} [A]
75.6	0.8
103.0	1.1
132.1	1.4
150.0	1.6
175.8	1.9
200.0	2.2
227.0	2.5

Table 2.1: Direct voltage and current measurements



Figure 2.15: Resistors bench

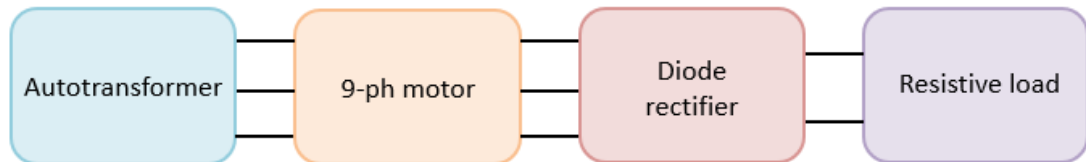


Figure 2.16: Test setup scheme

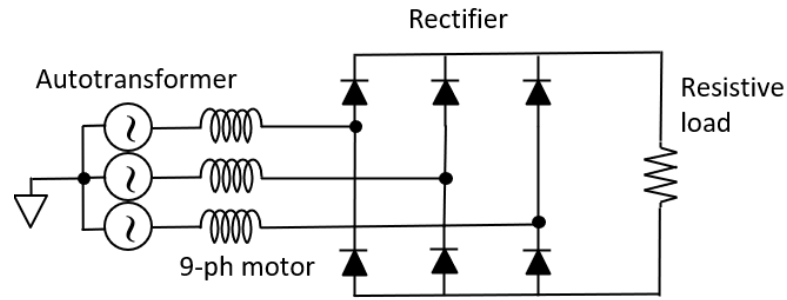


Figure 2.17: Test setup electrical scheme



Figure 2.18: Experimental setup with diode rectifier and resistive load

During the test, the motor was supplied with different voltage values at a grid frequency of $50Hz$. For each voltage/current value the rotor has been moved by rotating both clockwise and counterclockwise. The rotor was always stopped during the test phases. The test has been considered as successfully concluded.

Chapter 3

High Frequency Motor Model

Bearing current issue is well known for nearly 100 years, even if it is still difficult to manage [28].

Pulsewidth-modulation (PWM) AC motor drives require the usage of very high switching frequencies (up to tens of kilohertz) and so very fast switching devices such as silicon carbide (SiC) or gallium nitride (GaN) MOSFETs. These devices reduce converter losses, but they generate a common mode (CM) voltage with a very high dv/dt , which leads to a CM-current. The HF-CM-current is mainly conducted through the stator-winding stator-core capacitance, back to the source through the grounded machine housing. This causes the so-called circulating bearing current.

Failures caused by bearing currents could lead to several mechanical damages in electrical machines resulting in high maintenance costs. For automotive applications it must consider the additional problem of user safety, which is not possible to ensure when the extent of circulating currents became too high.

This specific configuration of the motor requires the mounting of the inverter directly on the motor housing, that introduces the ulterior risk to affect the switches commutation.

International standards impose to predict these phenomena considering the whole inverter, cables and motor system, but this thesis only focuses on the motor model. The aim of this section is to create a clear model of the bearing currents circulating in the motor housing.

To do this, several simulations based on bibliography, analytical calculations on motor geometries, measurements and the use of finite element softwares such as ANSYS were performed.

3.1 Lumped HF Parameters First Measurement

As written above, this chapter focuses on the HF model of the electric motor to be used in a PLECS simulation.

The starting point was a PLECS model that considers the motor like a RLE load (figure 3.1). It is not incorrect but a much more accurate model is needed to evaluate bearing currents.

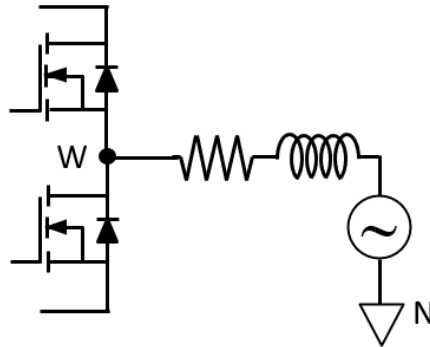


Figure 3.1: RLE one phase motor model

Bibliography offers several high frequency electric motor models. Following [29] and [30], phase-to-housing impedance was measured by using the layout shown in figure 3.2 for one of the nine phases, assuming an identical behaviour of the others. In particular:

- W = phase
- N = neutral point
- G = motor housing

Star center is indicated as in the figure because the particular multi three-phase structure of the motor offers the access to the three star centers. This would not be possible in three-phase solutions.

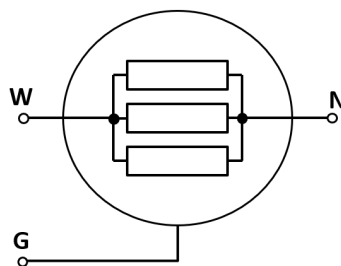


Figure 3.2: Connection layout for the phase-to-housing impedance measurements

HF motor parameters were identified through the frequency response of the phase-to-housing motor impedances as for the brushless machine cited in [29]. Measurements were performed in the range $1kHz - 1MHz$ using a programmable LCR meter (Hioki 3536, figure 3.3).



Figure 3.3: Hioki 3536 LCR meter

As discussed in [31] a HF lumped equivalent single-phase circuit can be designed as follows:

- L_d = phase leakage inductance
- C_g = capacitance representing the winding-to-ground distributed capacitances
- R_e = resistance representing eddy currents inside the magnetic core and the motor frame
- L_{se}, R_{se} = RL dipole modeling the skin effect

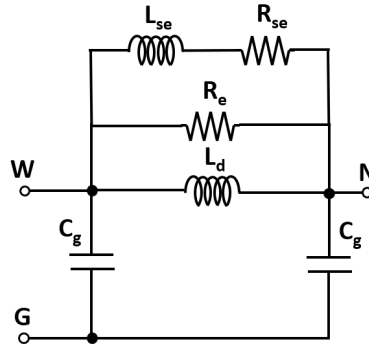


Figure 3.4: Single-phase HF equivalent circuit

Authors of [29] demonstrated that the parameters don't vary with the rotor position. A further test as in the case of torque evaluation was therefore considered superfluous in a first moment.

Differently from the case cited in the paper, for this brushless machine it is possible to

identify skin effect parameters because the three star centers are accessible.

From a practical point of view, it is necessary to select just one of the measured values, while the test brought to a thousand of measurements. As in the paper, values correspondent to the first resonance peak have been considered and listed in table 3.1:

Parameter	Value
L_d	442.94 <i>mH</i>
C_g	452.47 <i>pF</i>
R_e	2.75 <i>kΩ</i>
L_{se}	6.83 <i>μH</i>
R_{se}	2.80 <i>kΩ</i>

Table 3.1: HF lumped motor parameters

3.1.1 Further Considerations on Winding-to-Housing Capacitance C_g

A 3 mm thick layer of insulation (kapton [32]) was hypotesized and, as consequence, winding-to-housing capacitance was recomputed.

To evaluate the "new" winding-to-housing capacitance to be used in PLECS motor model basic plane capacitor formula was used.

Kapton dielectric constant is $\epsilon_r = 3.4$, while the external diameter of the motor is $d_{ext} = 140 \text{ mm}$ and the concentrated windings lenght is $L = 100 \text{ mm}$. Using the cylindrical capacitor formula 3.1:

$$C_g = \frac{2\pi\epsilon_0\epsilon_r L}{\ln \frac{r_{ext}}{r_{int}}} = 432 \text{ pF} \quad (3.1)$$

New capacitance was used for the PLECS simulation instead of the measured one.

3.2 PLECS First Draft Simulation

The new HF motor model was implemented in PLECS to evaluate the total current flowing in the motor housing (identified with the letter G).

The main problem of this case study is that neither the motor housing nor the inverter are connected to ground. Having a floating motor and inverter could bring to dangerous voltage oscillations with respect to the ground or bearing currents that could flow in the inverter legs (to close the loop). To be more precise, the model includes the stray capacitance between high and low legs of the inverter and the motor housing. This is necessary because of the particular positioning of the inverter.

Moreover, an extra resistive contribute is considered in order to take in count the amount of iron of the iron. A tooth-to-tooth resistance and an inverter-to-tooth resistance, which values were analitically calculated, are added to the model.

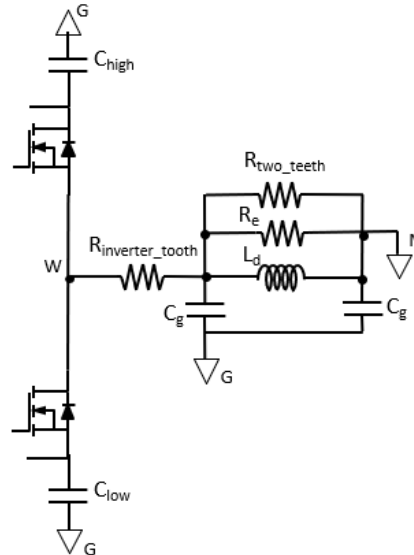


Figure 3.5: Complete HF inverter leg and motor model with analitically calculated impedances

Once implemented the model above, it is interesting to evaluate the total current flowing in the motor housing, as well as the voltage (and its oscillation) between the housing and the ground.

3.2.1 Total Current flowing in the Motor Housing

To evaluate this current, some amperometers were used.

Obviously, the sum of the currents in the nine phases is null, with currents flowing in the inverter legs of $0.27 - 0.29 A$ and currents in the two motor stray capacitance of $0.38 - 0.39 A$ and $0.007 - 0.18 A$. This difference in the motor model is reasonable because the right side of the model "suffers" the presence of a further impedance.

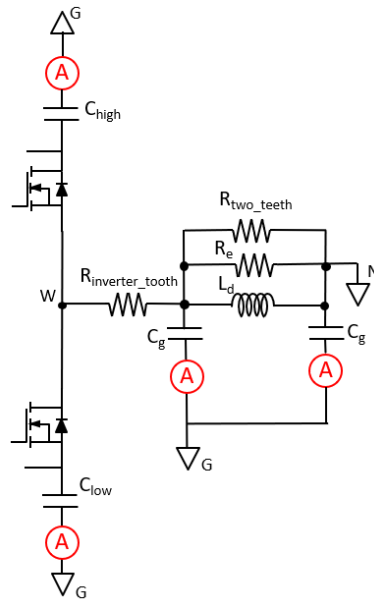


Figure 3.6: HF model with amperometers

3.2.2 Voltage between motor housing and ground

As written above, not only the currents must be evaluated. The oscillation of the housing-to-ground voltage is, in fact, one third of the DC-Link voltage.

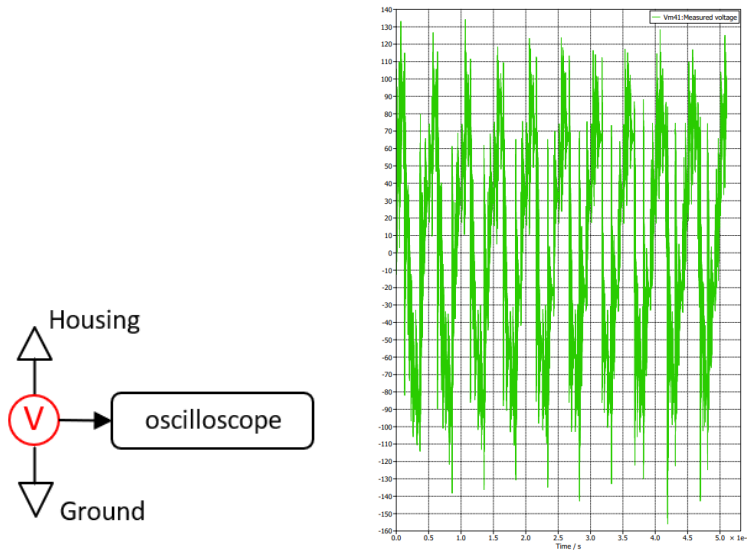


Figure 3.7: Voltage oscillations setup and plot

3.3 HF Motor Model Sweep Measurements

Considerations raised in the preceding paragraph have led to the need to create an even more precise model. LCR meter was used in the range $10\text{ kHz} - 1\text{ MHz}$ to measure the phase-to-housing impedance, phase-to-star center impedance and star center-to-housing impedance, as done in [29]. Sweep measurements provided 1000 measures in the cited range. The test was repeated for each phase. Results are coherent with the ones produced by the paper authors.

3.3.1 Impedance Measurements for each of the Nine Phases

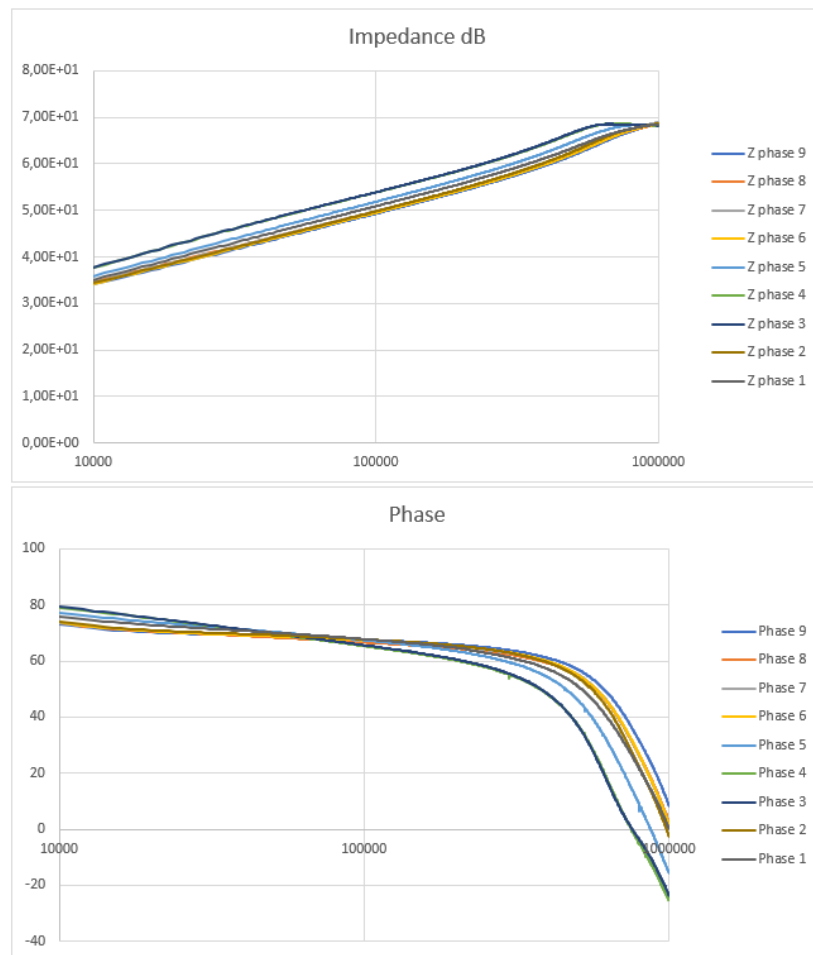


Figure 3.8: Phase-to-star center impedance, module and phase

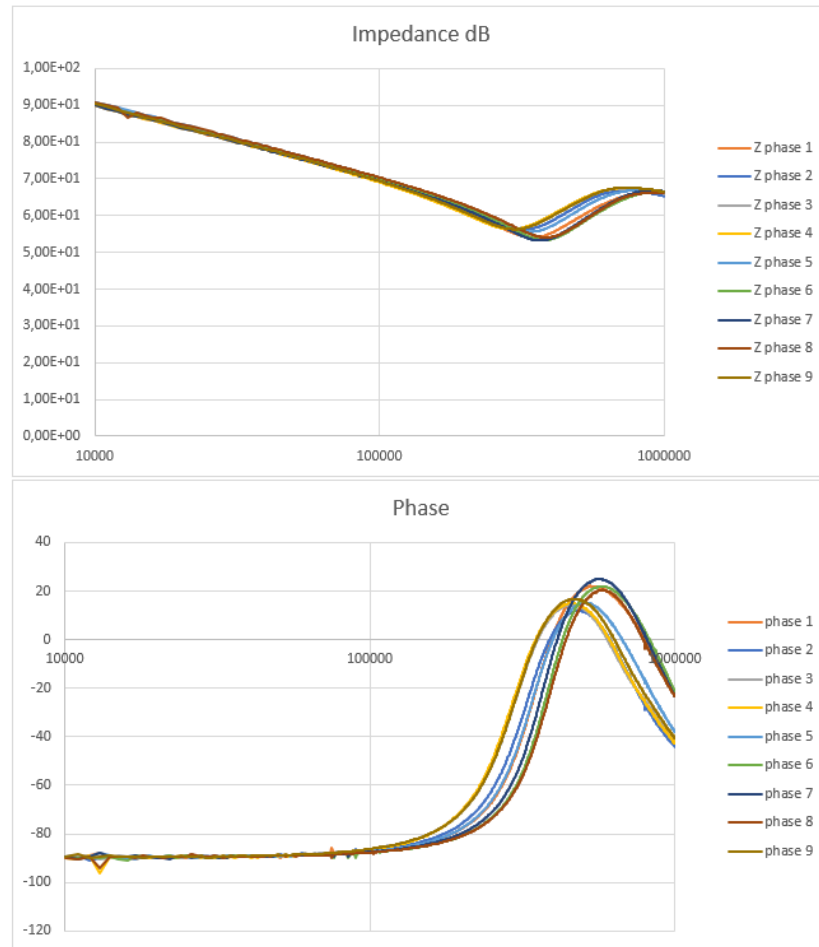


Figure 3.9: Phase-to-housing impedance, module and phase

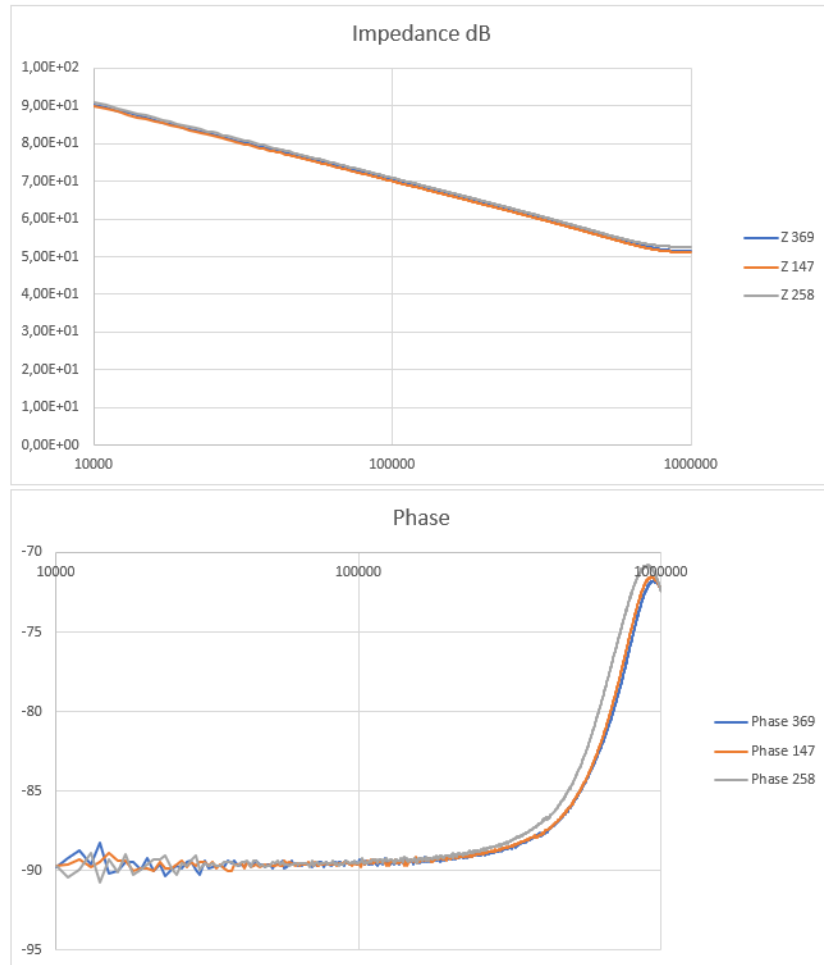


Figure 3.10: Star center-to-housing impedance, module and phase

It is evident a similar behavior of the phases. It is reasonable to attribute the same impedance value to every phase. To have a more precise evaluation of the impedance the same measurements are made on one phase for different positions of the rotor. The rotor is rotated by two electrical degrees to each test.

3.3.2 Impedance Measurements for One Phase and Different Rotor Positions

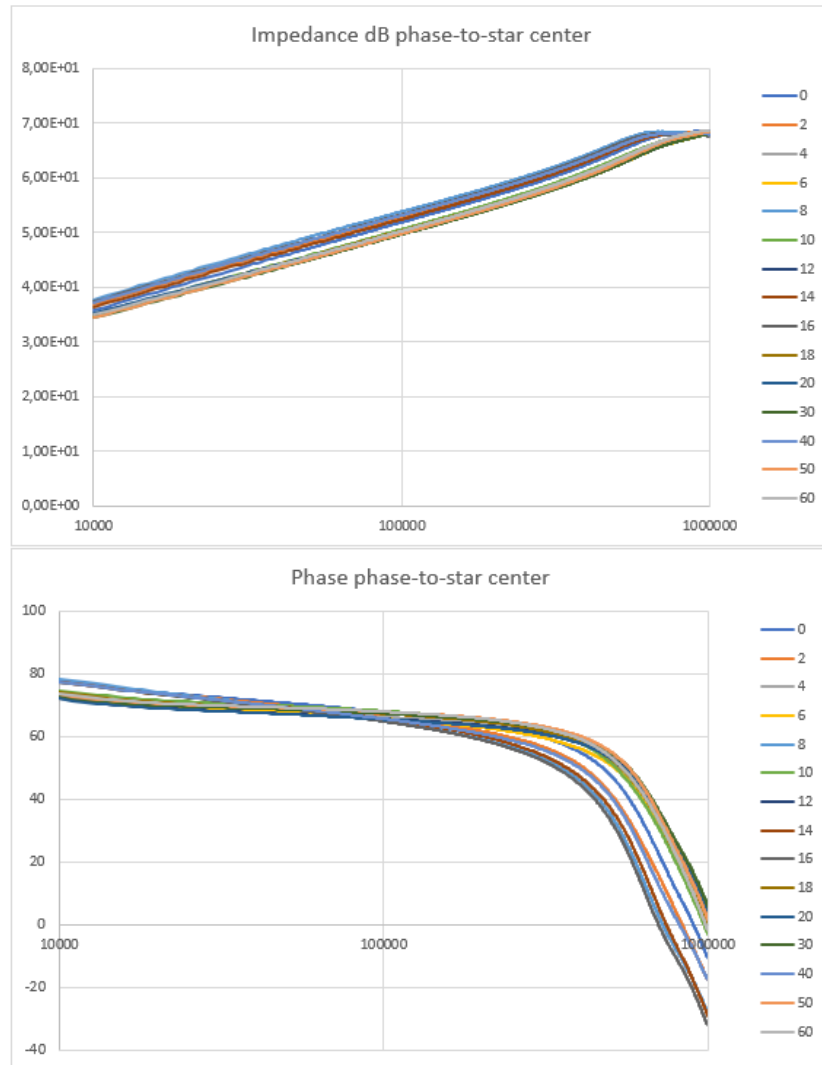


Figure 3.11: Phase-to-star center impedance, module and phase

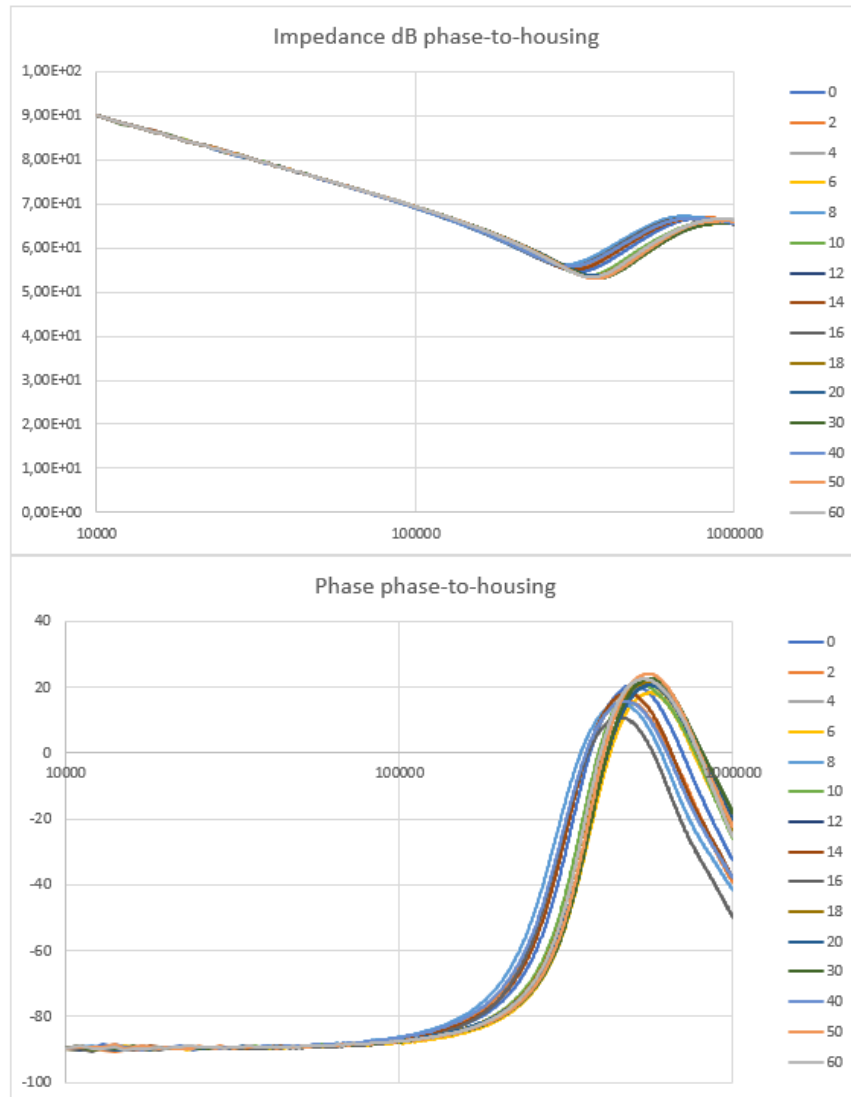


Figure 3.12: Phase-to-housing impedance, module and phase

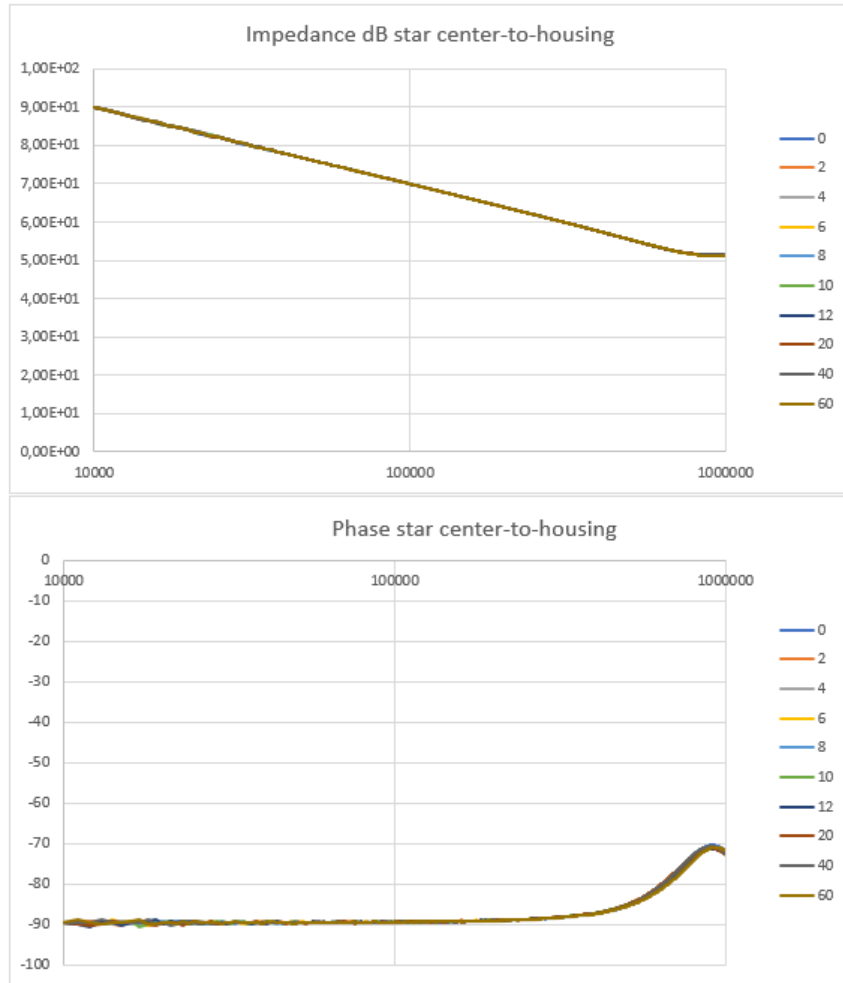


Figure 3.13: Star center-to-housing impedance, module and phase

It is once again evident the same behavior with some differences due to the rotor position. To have a satisfying PLECS model an average of the values obtained during the measurements was made. To do this, a 3D model of the measurements was produced.

3.3.3 3D Model of the Measurements, One Phase and Different Rotor Positions

2D models are not sufficient to model the impedances, that is why 3D models of the phase-to-housing and phase-to-star center measurements were produced. It is not necessary to do the same for the star center-to-housing because figure 3.13 evidences an identical behaviour for each of the rotor positions.

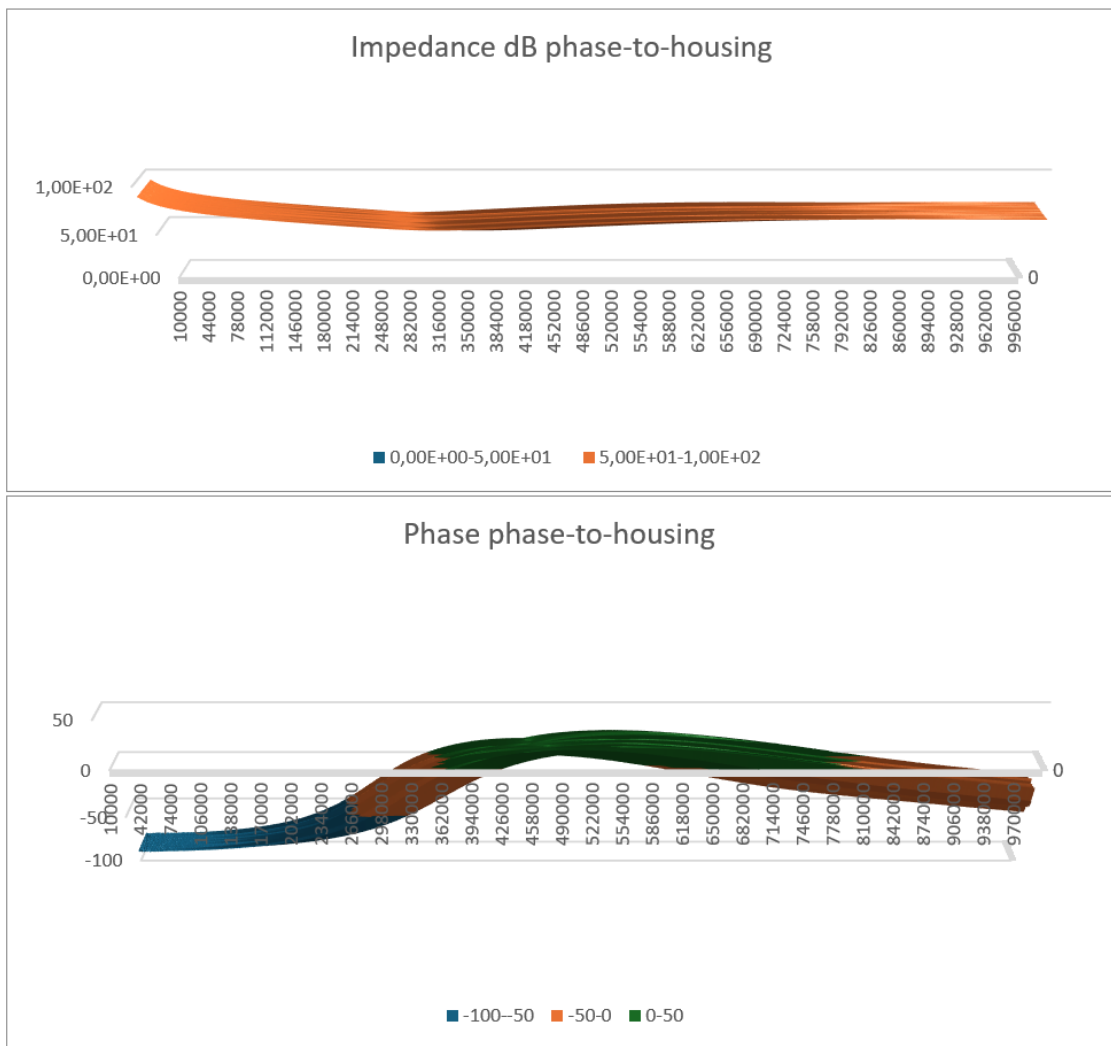


Figure 3.14: Phase-to-housing impedance 3D, module and phase

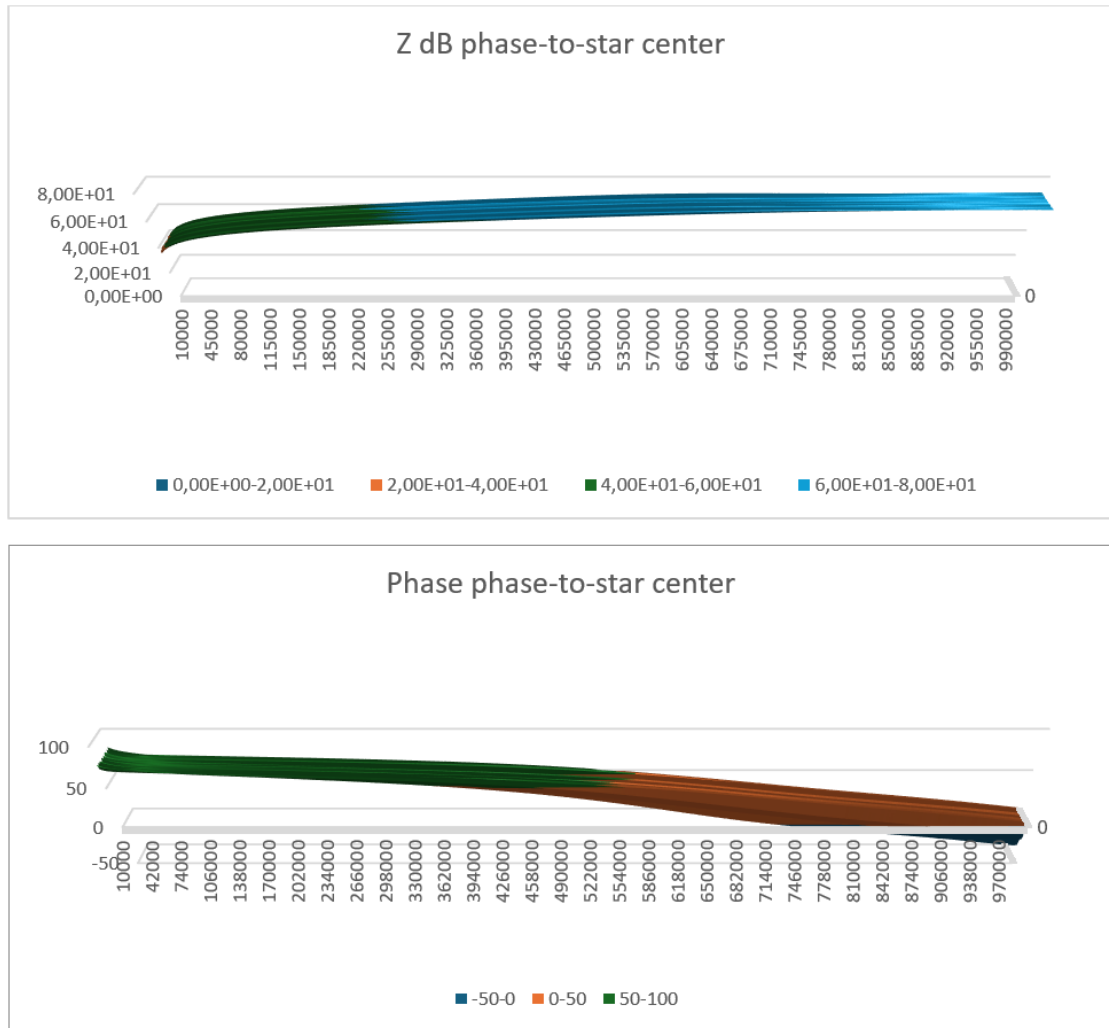


Figure 3.15: Phase-to-star center impedance 3D, module and phase

3.4 Approximated Model for PLECS Simulations using Passive Components based on Sweep Impedance Measurements and Foster Form

Introduction to RLC Bipole Synthesis Using Foster Form

In electrical engineering, the synthesis of RLC (Resistor-Inductor-Capacitor) circuits is a fundamental procedure used to design circuits that exhibit specified impedance characteristics over a range of frequencies. The Foster form is a well-established method for RLC circuit synthesis, particularly suited for creating circuits that replicate the

behavior of a given transfer function derived from experimental impedance and phase data. In this case, MATLAB scripts available in Appendixes C, D and E show how the experimental data were first approximated with a transfer function and then, using Foster Form, represented as RLC bipoles [33].

Foster Form Synthesis

The Foster form is a technique used to decompose a given impedance function into a sum of simpler impedances, each of which can be realized using basic RLC components. The principal idea behind the Foster form is to represent the impedance function as a series or parallel combination of resonant circuits, each characterized by its own resonant frequency and quality factor.

There are two primary types of Foster forms:

- **Foster I Form (Series):** This form represents the impedance as a sum of series resonant circuits. It is typically employed when the impedance function can be expressed as a sum of terms, each containing a pole at a specific frequency.
- **Foster II Form (Parallel):** This form represents the impedance as a sum of parallel resonant circuits. It is used when the impedance function can be decomposed into a sum of terms, each representing a parallel resonance.

Steps in Foster Form Synthesis

1. **Identify the Transfer Function:** The initial step in Foster form synthesis is to obtain the transfer function that describes the desired impedance characteristics. This transfer function can be derived from experimental data or specified as part of the design requirements.
2. **Partial Fraction Expansion:** The transfer function is then decomposed into partial fractions. This step involves expressing the transfer function as a sum of simpler fractions, each corresponding to a specific resonant frequency.
3. **Determine Component Values:** For each term in the partial fraction expansion, the corresponding R, L, and C values are calculated. These values are derived from the coefficients of the partial fractions and the poles and zeros of the transfer function.
4. **Realize the Circuit:** The calculated R, L, and C values are used to construct the RLC circuit. Depending on the form of the partial fraction expansion, the circuit will be a combination of series or parallel resonant circuits.

Practical Application

The practical application of Foster form synthesis is demonstrated through a case study where experimental impedance and phase data are used to derive a transfer function. This transfer function is then synthesized into an RLC circuit using the Foster form

method. The resulting circuit is analyzed to ensure that its impedance characteristics match the desired behavior.

By employing Foster form synthesis, engineers can design RLC circuits that precisely replicate the behavior of complex impedance functions. This method provides a systematic approach to circuit design, ensuring that the desired impedance characteristics are achieved over a specified frequency range.

The following sections detail the step-by-step procedure for Foster form synthesis, including the mathematical derivation of component values and the implementation of the synthesized circuit in MATLAB.

3.4.1 Phase - to - Star center Impedance

MATLAB script is available in appendix C. This script performs the following tasks:

1. **Loading Data:** The script starts by loading the frequency and impedance data.
2. **Conversion to Decibels:** It converts the impedance values to decibels for plotting the magnitude Bode plot.
3. **Transfer Function Definition:** The script defines an initial estimate of the transfer function $H(s) = K \cdot (s + \omega_z)$.
4. **RLC Equivalent Circuit with Foster form:** It defines an equivalent RLC solution using Foster form.
5. **Bode Plot Calculation:** It calculates the Bode plot (magnitude and phase) for the defined transfer function and RLC solution.
6. **Plotting:** The script plots the experimental data, the simulated transfer function data and RLC approximation data for both magnitude and phase.

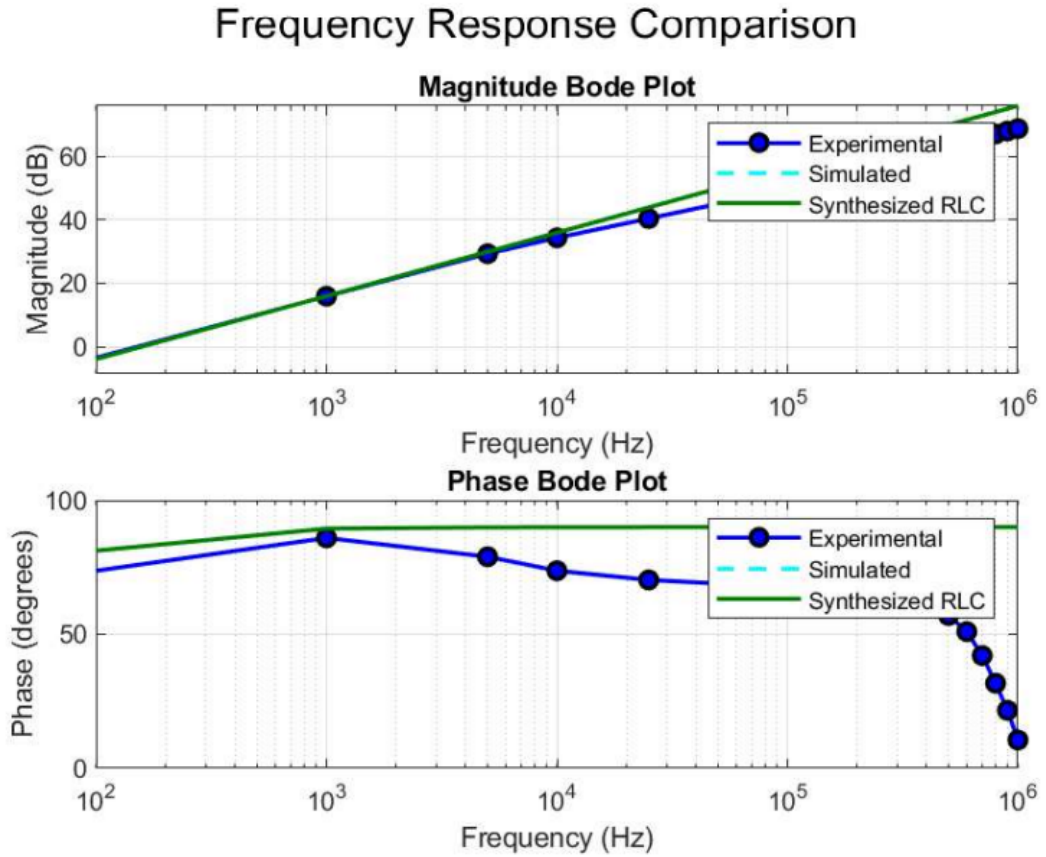


Figure 3.16: Phase-to-star center Impedance, experimental data and approximation

The approximated transfer function as calculated in MATLAB code is:

$$H(s) = 0.001s + 0.06283 \tag{3.2}$$

Foster Form Synthesis

In this first case it is quite simple to identify the components and their values.

Step 1: Identify Components

The transfer function components are identified as follows:

$$\begin{aligned} 0.001s &\rightarrow \text{Inductor } L \\ 0.06283 &\rightarrow \text{Resistor } R \end{aligned}$$

Step 2: Determine Values

The component values are:

$$R_{WN} = 62.830 \text{ m}\Omega$$

$$L_{WN} = 1 \text{ mH}$$

3.4.2 Phase - to - Housing Impedance

The script available in appendix D performs the following tasks:

1. **Loading Data:** The script starts by loading the frequency and impedance data.
2. **Conversion to Decibels:** It converts the impedance values to decibels for plotting the magnitude Bode plot.
3. **Transfer Function Definition:** The script defines an initial estimate of the transfer function $H(s) = \frac{K(s+w_{z1})(s+w_{z2})}{(s+w_{p1})(s+w_{p2})}$.
4. **RLC Circuit Definition:** Foster method to approximate the transfer function with some bipoles.
5. **Bode Plot Calculation:** It calculates the Bode plot (magnitude and phase) for the defined transfer function and RLC approximation.
6. **Plotting:** The script plots the experimental, the simulated transfer function and RLC approximation data for both magnitude and phase.

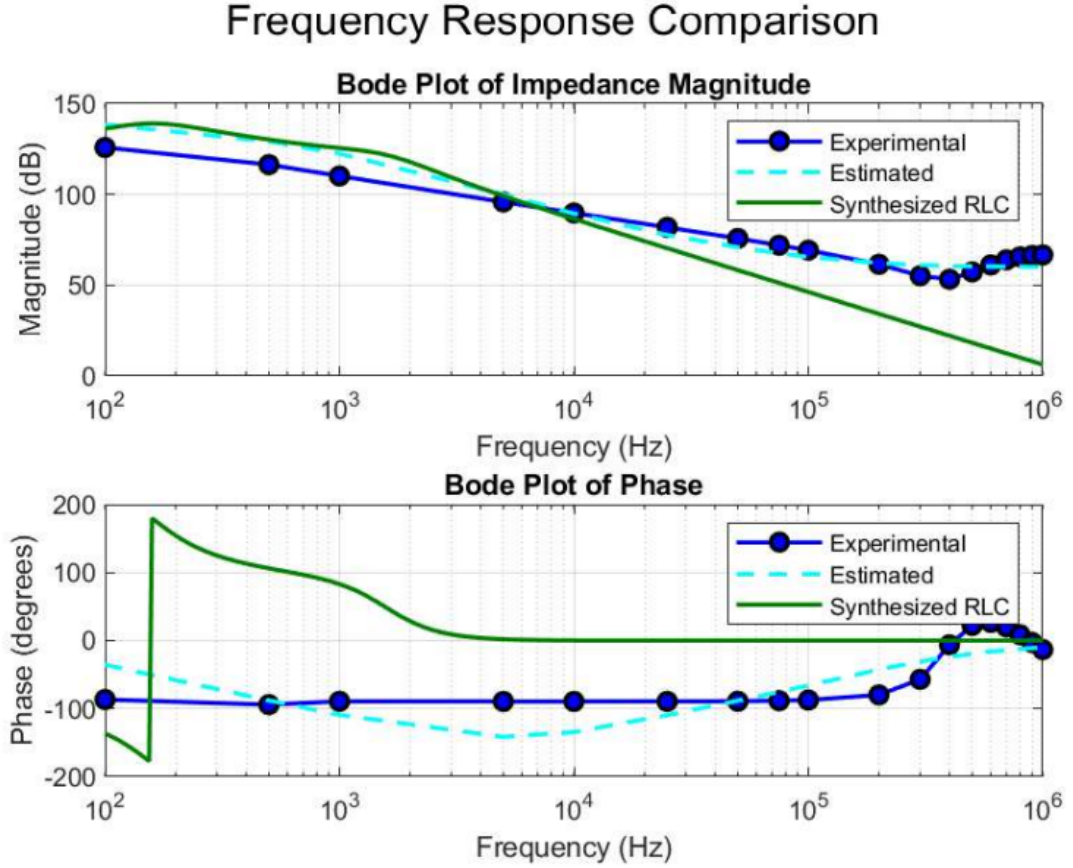


Figure 3.17: Phase-to-housing Impedance, experimental data and approximation

The transfer function $H(s) = \frac{K(s+w_{z1})(s+w_{z2})}{(s+w_{p1})(s+w_{p2})}$ can be realized using passive components.

$$H(s) = \frac{K(s^2 + (z_1 + z_2)s + z_1z_2)}{s^2 + (p_1 + p_2)s + p_1p_2} \quad (3.3)$$

where:

- $K = 10^3$
- $z_1 = 1 \times 10^6$ rad/s
- $z_2 = 1 \times 10^5$ rad/s
- $p_1 = 1 \times 10^3$ rad/s
- $p_2 = 1 \times 10^4$ rad/s

Substituting the given values, the transfer function becomes:

$$H(s) = \frac{1 \times 10^3(s^2 + 1.1 \times 10^6s + 1 \times 10^{11})}{s^2 + 1.1 \times 10^4s + 1 \times 10^7} \quad (3.4)$$

Foster Form Synthesis

Step 1: Partial Fraction Expansion

The transfer function is decomposed into partial fractions to identify the series RLC components:

$$H(s) = K \left(\frac{A}{s + p_1} + \frac{B}{s + p_2} \right) \quad (3.5)$$

Step 2: Solving for A and B

To solve for A and B , equate the coefficients:

$$K(s^2 + (z_1 + z_2)s + z_1z_2) = A(s + p_2) + B(s + p_1) \quad (3.6)$$

Solving for A and B , we get:

$$A = K \cdot \frac{z_1z_2p_1}{(p_1 - p_2)} \quad (3.7)$$

$$B = K \cdot \frac{z_1z_2p_2}{(p_2 - p_1)} \quad (3.8)$$

Substituting the given values, we get:

$$\begin{aligned} A &= 1 \times 10^3 \cdot \frac{(1 \times 10^6) \cdot (1 \times 10^5) \cdot (1 \times 10^3)}{(1 \times 10^3 - 1 \times 10^4)} \\ &= 1 \times 10^3 \cdot \frac{1 \times 10^{14}}{-9 \times 10^3} \\ &= 1.1111 \times 10^{10} \end{aligned}$$

$$\begin{aligned} B &= 1 \times 10^3 \cdot \frac{(1 \times 10^6) \cdot (1 \times 10^5) \cdot (1 \times 10^4)}{(1 \times 10^4 - 1 \times 10^3)} \\ &= 1 \times 10^3 \cdot \frac{1 \times 10^{15}}{9 \times 10^3} \\ &= 1.1111 \times 10^{11} \end{aligned}$$

Step 3: Calculate R , L , and C Values

Using the values of A and B , calculate the R , L , and C values for the synthesized RLC circuit.

For the first term:

$$\begin{aligned} R_{WG1} &= A = 11.111 \text{ G}\Omega \\ C_{WG1} &= \frac{1}{p_1 R_1} = \frac{1}{(1 \times 10^3) \cdot (11.111 \times 10^9)} = 0.009 \text{ pF} \\ L_{WG1} &= \frac{R_1}{p_1} = \frac{11.111 \times 10^9}{1 \times 10^3} = 11.111 \text{ MH} \end{aligned}$$

For the second term:

$$R_{WG2} = B = 111 \text{ G}\Omega$$

$$C_{WG2} = \frac{1}{p_2 R_2} = \frac{1}{(1 \times 10^4) \cdot (111 \times 10^9)} = 9.001 \times 10^{-17} \text{ F}$$

$$L_{WG2} = \frac{R_2}{p_2} = \frac{1.1111 \times 10^{11}}{1 \times 10^4} = 11.111 \times \text{MH}$$

The synthesized RLC circuit consists of two series RLC circuits connected in parallel to achieve the desired impedance characteristics. Each series RLC circuit represents one of the partial fraction terms from the decomposition of the transfer function.

3.4.3 Star center - to - Housing Impedance

MATLAB script is once again available in appendix E. This script performs the following tasks:

1. **Loading Experimental Data:** The script starts by loading the frequency, impedance, and phase data.
2. **Conversion to Decibels:** It converts the impedance values to decibels for plotting the magnitude Bode plot.
3. **Approximate Transfer Function Definition:** The script defines an initial estimate of the transfer function $H(s) = \frac{K(s+w_{z1})}{(s+w_{p1})(s+w_{p2})}$.
4. **RLC Equivalent Circuit** It calculates the total impedance of the equivalent circuit.
5. **Bode Plot Calculation:** It calculates the Bode plot (magnitude and phase) for the defined transfer function.
6. **Plotting:** The script plots the experimental data, the simulated transfer function and the RLC transfer function for both magnitude and phase.

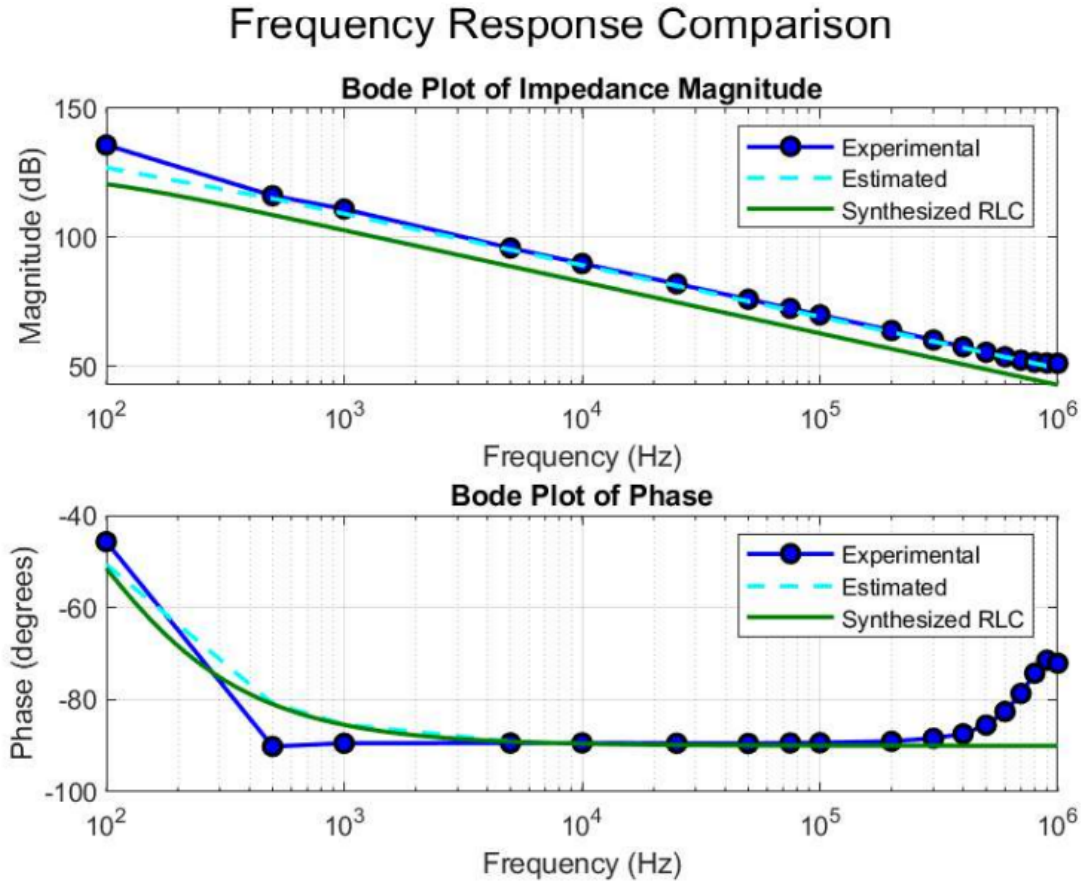


Figure 3.18: Star center-to-housing Impedance, experimental data and approximation

Synthesis of RLC circuit using Foster Form

The parameters for the transfer function derived from matlab script are:

- $K = 1.8 \times 10^9$
- $z_1 = 1 \text{ rad/s}$
- $p_1 = 10 \text{ rad/s}$
- $p_2 = 500 \text{ rad/s}$

$$H(s) = \frac{1.8 \times 10^9(s + 1)}{(s + 10)(s + 500)} \quad (3.9)$$

Partial Fraction Expansion

The transfer function is decomposed into partial fractions to identify the series RLC components.

$$H(s) = \frac{1.8 \times 10^9(s+1)}{(s+10)(s+500)} = \frac{A}{s+10} + \frac{B}{s+500} \quad (3.10)$$

To solve for A and B , multiply through by the common denominator and equate coefficients:

$$1.8 \times 10^9(s+1) = A(s+500) + B(s+10) \quad (3.11)$$

Substituting appropriate values for s :

- Let $s = -10$:

$$1.8 \times 10^9(-10+1) = A(-10+500) \quad (3.12)$$

$$A = \frac{1.8 \times 10^9(-9)}{490} = -3.3061 \times 10^7 \quad (3.13)$$

- Let $s = -500$:

$$1.8 \times 10^9(-500+1) = B(-500+10) \quad (3.14)$$

$$B = \frac{1.8 \times 10^9(-499)}{-490} = 1.8337 \times 10^9 \quad (3.15)$$

Thus, the partial fractions are:

$$H(s) = \frac{-3.3061 \times 10^7}{s+10} + \frac{1.8337 \times 10^9}{s+500} \quad (3.16)$$

Realization of Each Term as RLC Components

Each term in the partial fraction expansion can be realized as a series RLC circuit.

- **First Term** $\frac{-3.3061 \times 10^7}{s+10}$: This term represents a parallel RC circuit, but due to the negative sign, it requires an alternative interpretation. For illustration purposes, if an ideal negative resistor is assumed:

$$R_{NG1} = 33.061 \text{ M}\Omega \quad (3.17)$$

$$C_{NG1} = \frac{1}{10 \cdot |R_1|} = 3.02 \text{ nF} \quad (3.18)$$

- **Second Term**: $\frac{1.8337 \times 10^9}{s+500}$: This term represents a series RL circuit:

$$R_{NG2} = 1.8337 \text{ G}\Omega \quad (3.19)$$

$$L_{NG2} = \frac{R_2}{500} = 3.6674 \text{ MH} \quad (3.20)$$

The two branches, each corresponding to one of the partial fraction terms in the transfer function, are in parallel. This is because each term in the partial fraction expansion represents a separate path for current, which is a characteristic of a parallel circuit.

3.5 Conclusion oh High Frequency Motor Model

This sections detailed the synthesis of an RLC circuit using the Foster form for the given transfer function $H(s)$. The steps included partial fraction expansion and realization of each term as RLC components, followed by MATLAB implementation for frequency response analysis.

Final passive components motor model for high frequencies is the following:

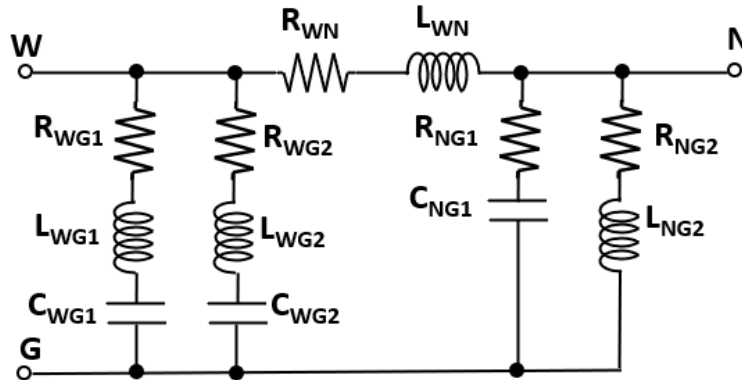


Figure 3.19: High frequency motor model for PLECS simulation

Chapter 4

ANSYS Motor Model for Parasitic Capacitances and FEMM 4.2 Dielectric Losses Evaluation

The aim of this chapter is to validate the considerations formulated in Chapter 3 and bring the model to a more complex one by inserting the Cool-X cooling device. ANSYS ELECTRONICS suite is used for the purpose. It is a comprehensive platform where it's possible to design and simulate different 2D and 3D configurations, in our case in electromagnetic domain. The procedure to build a reasonable model of an electric machine is described in the following paragraphs.

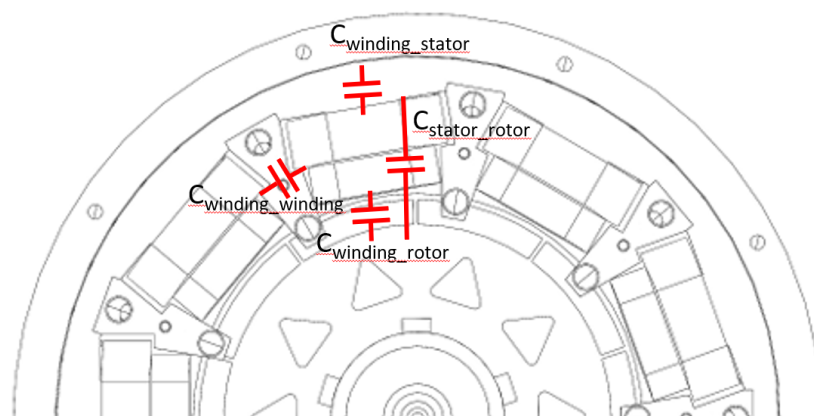


Figure 4.1: Parasitic capacitances schematic

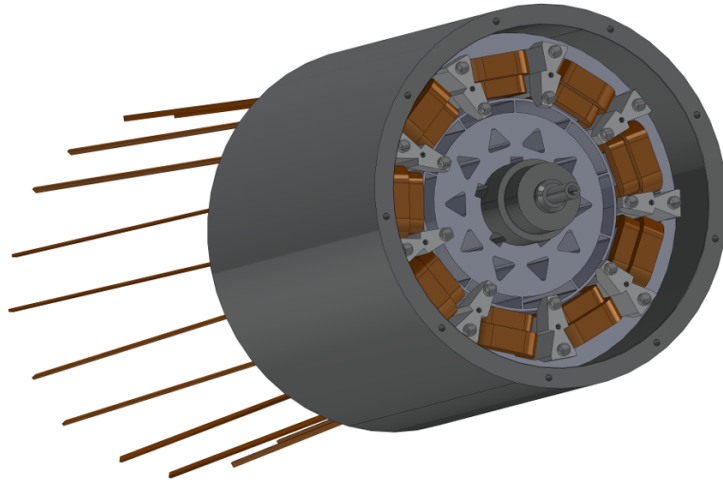


Figure 4.2: CAD design of the motor

4.1 Ansys Maxwell Introduction

ANSYS is a comprehensive simulation software suite used widely in engineering for its advanced capabilities in modeling, analyzing, and solving complex structural, thermal, and electromagnetic problems. One of the core techniques utilized by ANSYS is the Finite Element Method (FEM), a numerical technique for finding approximate solutions to boundary value problems for partial differential equations.

The Finite Element Method works by dividing a large problem into smaller, simpler parts called finite elements. The original complex geometry is discretized into a mesh of elements, each of which is governed by equations derived from the underlying physical laws. These elements are interconnected at points called nodes. By solving the equations for each element and assembling them into a global system, FEM can approximate the behavior of the entire system. This method is particularly powerful because it can handle complex geometries and boundary conditions that are otherwise difficult to solve analytically.

In ANSYS, the process begins with pre-processing, where the geometry is defined and the mesh is generated. The software offers tools to refine the mesh for higher accuracy, including adaptive meshing that automatically adjusts the mesh based on the solution's requirements. Material properties and boundary conditions are then applied to the model. Once the pre-processing is complete, the solution phase begins, where ANSYS solves the assembled equations using various numerical solvers optimized for different types of analyses. Post-processing involves visualizing the results, where users can inspect stress distributions, temperature gradients, electromagnetic fields, and other parameters of interest.

ANSYS Electronics specifically focuses on the simulation of electromagnetic fields and their interaction with physical structures and materials. This suite includes tools for electromagnetic, circuit, and system simulation, addressing a broad range of applications from RF and microwave to power electronics and signal integrity.

One of the key tools within ANSYS Electronics is Maxwell, which focuses on low-frequency electromagnetic field simulation. Maxwell uses both FEM and the Finite Element-Boundary Integral (FE-BI) method for solving static, frequency-domain, and time-varying electromagnetic fields. It is essential for designing electric machines, transformers, sensors, and other devices where magnetic fields and induced currents are of primary concern. Maxwell can simulate the behavior of these devices under various operating conditions, providing insights into parameters such as magnetic flux distributions, eddy current losses, and inductance calculations. This is particularly important in optimizing the design for efficiency, performance, and reliability.

Maxwell's ability to couple electromagnetic simulations with thermal and structural analyses further enhances its utility. For instance, in the design of electric motors, it can simulate the electromagnetic performance, predict heating due to losses, and assess the structural impact of thermal expansion. This integrated multi-physics approach allows engineers to optimize the motor design holistically, ensuring that all aspects of performance are considered.

The integration of these tools within the ANSYS Electronics suite allows for a multi-physics approach, where thermal, structural, and electromagnetic analyses can be coupled to provide a holistic view of the performance and reliability of electronic devices. This capability is particularly valuable in the design of modern electronic systems, where the interaction between different physical phenomena can significantly impact the overall performance.

In summary, ANSYS leverages the Finite Element Method to provide powerful and versatile simulation capabilities. ANSYS Electronics extends these capabilities to the electromagnetic domain, offering specialized tools like Maxwell for low-frequency electromagnetic field simulations. This suite is invaluable for engineers looking to design and optimize complex electronic devices and systems.

4.2 Finite Element Analysis (FEA) Method and Energy Error

Finite Element Analysis (FEA) is a computational method used to approximate solutions to complex structural, thermal, and electromagnetic problems. It works by breaking down a large problem into smaller, manageable finite elements, which are interconnected at nodes. The behavior of each element is governed by equations derived from physical

laws.

One crucial aspect of FEA is the concept of energy error, which measures the difference between the exact solution and the approximate solution provided by the finite element model. The energy error quantifies the total potential energy discrepancy in the system, encompassing both strain energy in structural problems and electromagnetic energy in field problems. Minimizing this error is essential for achieving high-accuracy simulations. Adaptive meshing techniques are often employed to refine the mesh in regions with high energy error, enhancing the precision of the overall solution. This iterative process ensures that the FEA model converges to an accurate representation of the physical problem.

Referring in particular to the case in question, an energy error maximum of 1% is accepted. The simulation will be considered therefore concluded with success once the error will be come down under this level.

4.3 Parasitic Capacitances Evaluation

4.3.1 First Model of the Motor

Motor geometry is very complex to be analysed in a FEM simulations, that is why it is possible to simplify the model by reaching different grades of approximation.

The motor CAD cannot be imported directly into ansys, this resulted in the need to redesign the machine within the software. To facilitate simulations, the rotor was initially excluded from the model, as were the Cool-x devices. The model only focuses on the stator and on the concentrated windings.

For what that concerns these lasts, it is clear that the copper wire used to wound the windings was insulated by a coating. This tiny layer of insulation could not be represented as the windings were designed like single massive elements. For this reason one of the approximations cited above provides the representation of the coating as a 0.5 *mm* mylar envelope, whose datasheet is available in Appendix B.

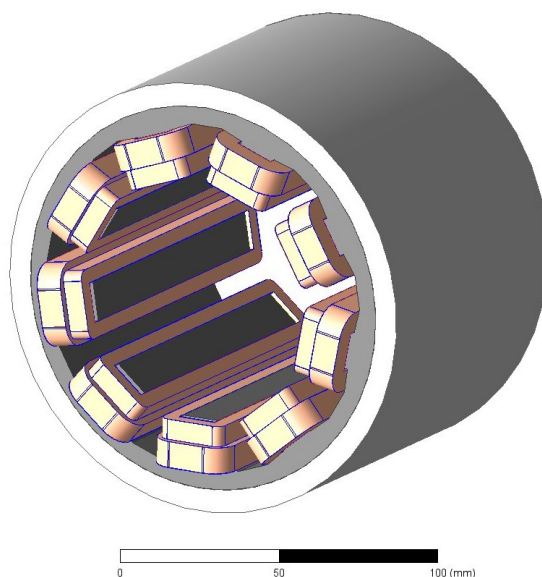


Figure 4.3: Stator and insulated windings motor model

Position	C [pF]
No insulating coating	
<i>Winding – to – winding</i>	2
<i>Winding – to – stator</i>	174
With insulating coating	
<i>Winding – to – winding</i>	2.2
<i>Winding – to – stator</i>	246

Table 4.1: Stator and concentrated windings parasitic capacitances

Meshing Size Importance

In ANSYS Electronics Maxwell simulations, the meshing size plays a crucial role in determining the accuracy and efficiency of the results. The mesh refers to the discretization of the geometry into smaller, finite elements over which the electromagnetic fields are computed. The dimensions of these mesh elements are vital because they directly influence the precision of the simulation outcomes.

A finer mesh, with smaller elements, tends to provide more accurate results by capturing the intricate variations in the electromagnetic fields more precisely. This is especially important in regions with high field gradients or complex geometries. However, finer

meshes also significantly increase computational resources and time. Conversely, a coarser mesh, with larger elements, reduces the computational load but may lead to less accurate results, potentially missing critical details in the fields.

The relationship between the size of the object and the size of the mesh elements is crucial. If the mesh elements are too large relative to the object, especially in areas with small or detailed features, the simulation may not capture these features accurately. This can lead to significant errors in the predicted electromagnetic behavior. Conversely, excessively small mesh elements for large objects can lead to unnecessary computational expense without substantial gains in accuracy.

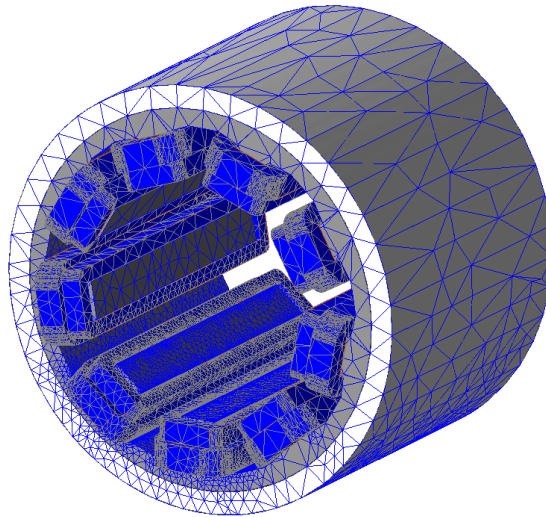


Figure 4.4: Mesh of the motor model

Inadequate meshing can lead to several issues. If the mesh is too coarse, it might not resolve important features of the electromagnetic fields, leading to inaccurate or incomplete analysis. This can result in erroneous predictions of device behavior, impacting the design and performance evaluations. Additionally, poorly defined mesh transitions between regions of different mesh densities can introduce numerical errors, affecting the convergence and stability of the solution.

Therefore, achieving an optimal balance in meshing size relative to the object's dimensions is essential. It ensures accurate simulations while managing computational resources effectively, enabling reliable and efficient analysis of electromagnetic phenomena in ANSYS Electronics Maxwell.

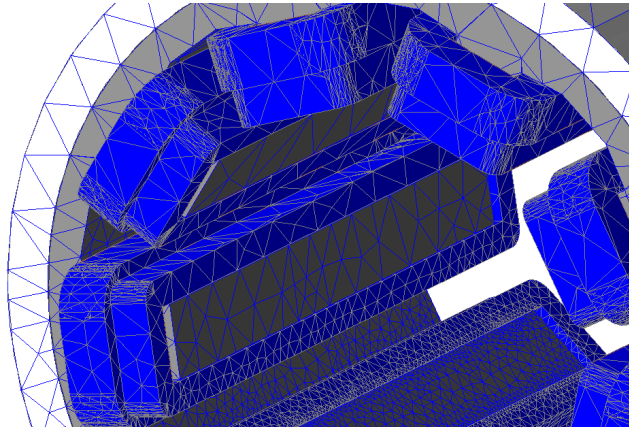


Figure 4.5: Mesh detail

4.3.2 Cool-X Motor Model

An upgrade of the model is made by adding the device called Cool-X: a 3D printed aluminium device designed to act as a in-cave heatsink.

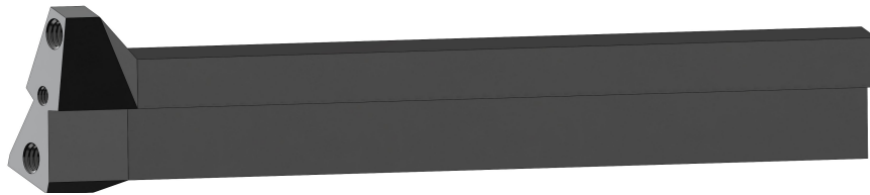


Figure 4.6: Cool-X device

In-cave Heatsink

An in-cave heatsink in electric motors is an innovative cooling solution designed to enhance thermal management and efficiency. Positioned internally within the motor, this heatsink dissipates heat generated during operation, maintaining optimal temperatures and preventing overheating. By integrating the heatsink directly into the motor's structure, it allows for effective heat transfer from the critical components, such as the stator and rotor, to the cooling fins.

This approach improves the motor's performance and longevity, as excessive heat can degrade insulation, reduce magnetic properties, and cause premature failure. The in-cave heatsink design optimizes space within the motor casing, enabling compact and efficient motor designs without compromising cooling capabilities. Such thermal management is crucial in high-performance applications, including electric vehicles and industrial machinery, where maintaining efficiency and reliability is paramount.

The effectiveness of in-cave heatsinks underscores the importance of advanced cooling technologies in enhancing the durability and efficiency of modern electric motors.

Cool-X Approximation

It is not necessary to totally represent the Cool-X device to obtain a satisfying model to be used in Ansys. For this reason, only the linear part of the device is included in the model, ignoring the part which stands outside of the cave.

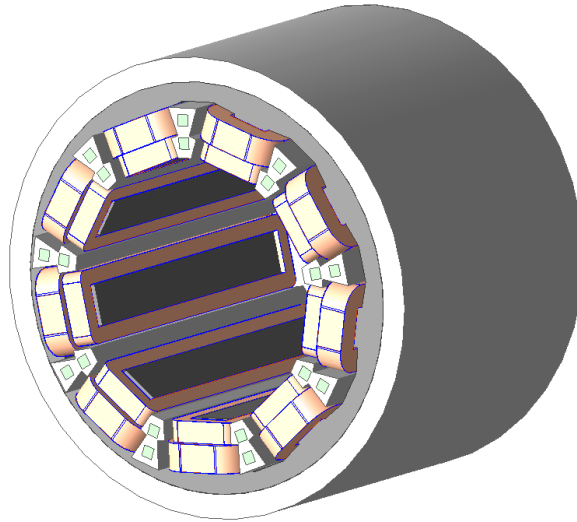


Figure 4.7: Motor model including Cool-X devices

As the chosen cooling liquid is an aqueous solution of ethylene glycol (50%), its dielectric properties must be considered. In particular it has a dielectric constant of 55 and a dielectric loss tangent of 0.8.

By adding the Cool-X device capacity between coil and coil can no longer be considered and it must be replaced with a series of two capacitances between winding and Cool-X.

The new capacitances are listed below. Capacitances could be considered neglectables when the dielectric fluid flows inside Cool-X devices.

4.3.3 Complete Motor Model

At last, the rotor was finally included in the model. It was not easy to complete the simulation because of the difficulty in modelling curved profiles in Ansys. Some geometries have therefore been simplified.

Position	C [pF]
<i>Winding – to – Cool – X</i>	25
<i>Stator – to – Cool – X</i>	22
<i>Winding – to – winding</i>	125
<i>Rotor – to – stator</i>	23
<i>Rotor – to – winding</i>	85
<i>Winding – to – stator</i>	246
<i>Winding – to – starcenter</i>	8

Table 4.2: Parasitic capacitances considering Cool-X device

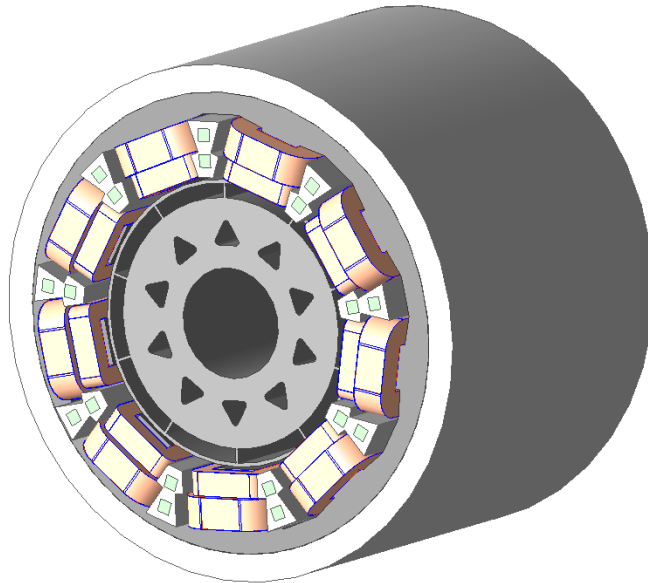


Figure 4.8: Complete motor model

4.4 Dielectric Losses in Cool-X Device

Since the cooling liquid inside Cool-X devices flows slowly with respect to the switching frequency of the inverter, dielectric losses at the device heads are evaluated in a static case with a good approximation.

As the aluminium is obviously equipotential, it is not necessary to also evaluate the losses inside the device because they are null.

Antifreeze and coolants are vital in automotive applications to prevent engine overheating and freezing. They enhance heat transfer, protect against corrosion, and maintain optimal engine temperature. Common types include ethylene glycol, which is the most used, propylene glycol, and silicone-based coolants, each offering specific dielectric properties essential for electric vehicle safety and performance.

Key points of coolant liquids are the following:

- **Dielectric Constant:** It is a measure of a material's ability to store electrical energy in an electric field. Higher values indicate better insulating properties.
- **Dielectric Loss Tangent:** This measures the energy dissipation of the dielectric material. Lower values indicate less energy loss and better efficiency.

4.4.1 Dielectric Properties of Ethylene Glycol 50% Solution

Ethylene glycol is commonly used as an antifreeze and coolant in automotive applications, particularly in a 50% aqueous solution. Here are the dielectric properties for a 50% ethylene glycol solution:

- **Dielectric Constant:** Approximately 50 at 25°C
- **Dielectric Loss Tangent:** Approximately 0.1

These properties are essential for ensuring that the ethylene glycol solution can effectively prevent freezing and overheating while maintaining electrical insulation in automotive systems.

Key Points

- **Dielectric Constant:** The dielectric constant of a 50% ethylene glycol solution is relatively high, which indicates its good insulating properties. This makes it suitable for use in automotive cooling systems, particularly in electric vehicles where electrical insulation is crucial.
- **Dielectric Loss Tangent:** The dielectric loss tangent indicates how much energy from the electric field is lost as heat. A value of 0.1 is moderate, suggesting that while there is some energy loss, the solution still performs efficiently as an insulator.

These properties are essential for ensuring the ethylene glycol solution can effectively prevent freezing and overheating while maintaining electrical insulation in automotive systems.

4.4.2 Dielectric Properties of Other Commercial Coolants

Common alternatives to ethylene glycol include propylene glycol, glycerin, and silicone-based coolants, each offering specific dielectric properties essential for electric vehicle safety and performance.

Dielectric Properties of Common Coolants

Propylene Glycol

- **Dielectric Constant:** Approximately 37 at 25°C
- **Dielectric Loss Tangent:** 0.05

Glycerin

- **Dielectric Constant:** Approximately 47 at 25°C
- **Dielectric Loss Tangent:** 0.1

Silicone-based Coolants

- **Dielectric Constant:** Varies, typically around 2.8 to 3.8
- **Dielectric Loss Tangent:** Approximately 0.0004 to 0.001

4.4.3 Dielectric Losses Evaluation for a 50% Ethylene Glycol Solution and Comparison with Other Coolants

The simulation was performed with a FEMM 4.2 current flow problem assigning the $\pm 200V$ of the DC-Link as conductor properties. The cooling channel filled with coolant was designed with a square equivalent section of 3.5 mm.

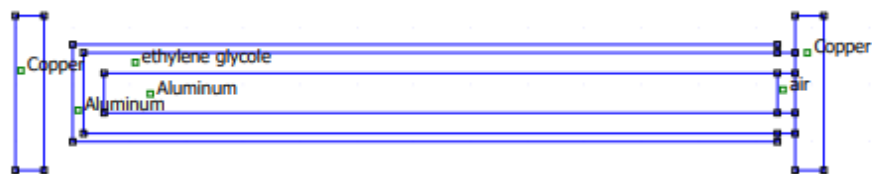


Figure 4.9: FEMM 4.2 simulation complete setup for dielectric losses evaluation

To simplify the simulation the aluminium part filled with coolant was eliminated, since it is equipotential and so free from dielectric losses.

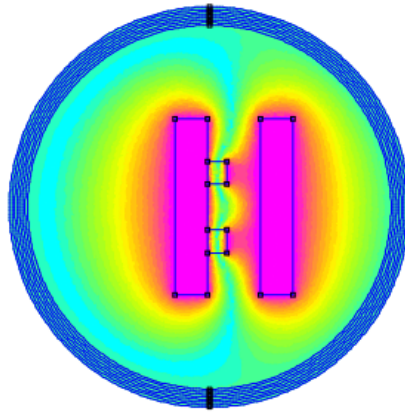


Figure 4.10: FEMM 4.2 simulation simplified setup for dielectric losses evaluation

The evaluated losses are neglectables but listed below with other coolants.

Coolant	Dielectric losses [mW]
Ethylene glycol	0.11
Propylene Glycol	0.08
Glycerin	0.12
Silicone-based coolants	0.008

Table 4.3: Dielectric losses in Cool-X devices using different coolants

Chapter 5

Assembly of a Liquid-Cooled Motor Version (Cool-X)

As written above, during the development of this thesis a new version of the motor was assembled. This particular version of the motor provides the liquid cooling by using aluminium 3D printed heat sinks placed inside the motor.

The first step involved the extraction of the rotor and the insertion of new coils inside the stator. Once the windings were positioned, it was Cool-X devices turn.

As Cool-X devices were 3D printed with rough surfaces and sharp edges, there was the concrete possibility to damage the windings during the positioning of the devices. For this reason, every cooling devices were hand-polished and covered with spray insulator for printed circuit boards.

5.1 Insulation Test

Unfortunately, it was not sufficient and some of the windings were damaged. It was possible to see the damages with an insulation test. Insulation tests in electric motors are essential for assessing the integrity of the insulation system, which is critical for the motor's safe and efficient operation. Some key technical aspects of insulation tests as indicated in standard **IEEE Std 43** follow:

- **Purpose:** To measure the resistance between the motor windings and the motor frame (ground). High resistance indicates good insulation.
- **Procedure:** A high DC voltage (typically 500V, 1kV, or higher) is applied using an insulation resistance tester (megohmmeter). The resistance is measured in megohms ($M\Omega$).
- **Expected Values:** Generally, a minimum insulation resistance of 1 $M\Omega$ per kV of operating voltage plus 1 $M\Omega$ is considered acceptable.

- **Equipment:** Megohmmeter is used for insulation resistance, PI, and DAR tests. It applies a high DC voltage and measures resistance.

Insulation tests were conducted at a voltage of 1 and, in case of complete insulation, the megohmmeter shows a higher than $11G\Omega$ resistance. In case of damaged windings, instead, the resistance resulted null or extremely low.

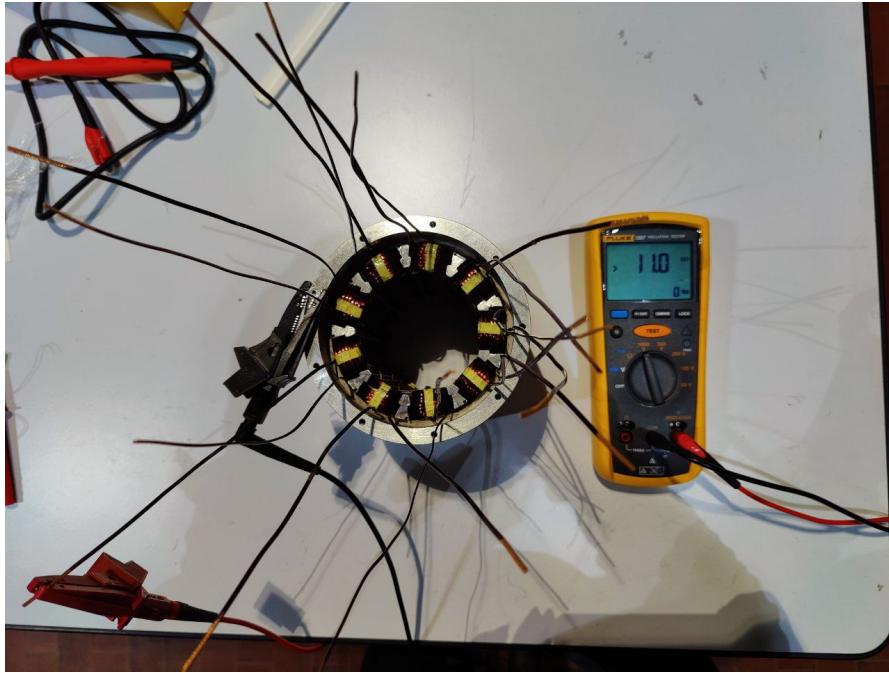


Figure 5.1: 1000 V insulation test on the motor

Damaged windings were so repaired with kapton tape. Also Cool-X devices were insulated with kapton until the total insulation was restored.

5.2 Connection of the Three Star Centers and Winding-to-Cool-X Connection

To cool down the motor is not the only function of Cool-X. Devices are also used to electrically connect the inverter to the windings. For this reason it was necessary to study a way to physically make this connection.

In a first moment the project planned to frame the winding terminal to the device. Unfortunately it was not a robust solution. That is why an alternative solution was found by drilling with M3 screws the devices up to a depth of 3.5 mm . As the processing was complex and extreme precision was required due to the limited space available in the

device, the work was done in DIGEP department.

Once the devices were ready, some lugs were made manually and soldered to one end of the windings, as shown in figure 5.2

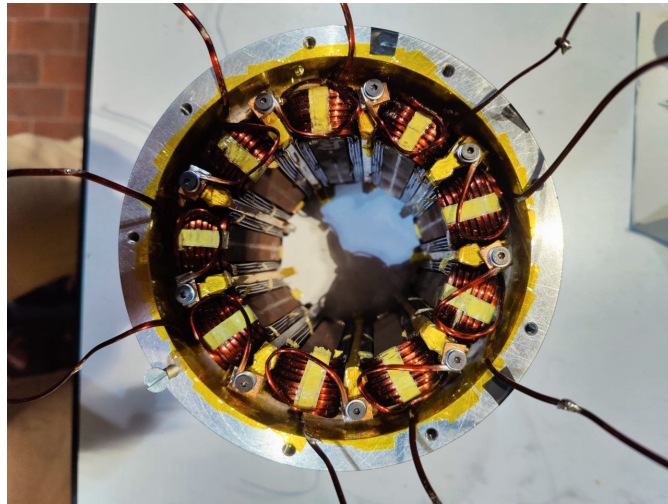


Figure 5.2: Windings-to-Cool-X connection

Another challenge was finding a way to connect the three star centers as the available space was reduced. Phases were bent to form a ring, welded together and then insulated with kapton tape.

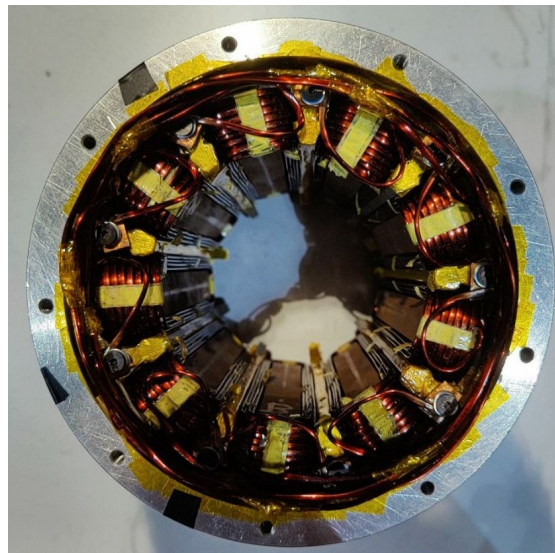


Figure 5.3: Star-center connection

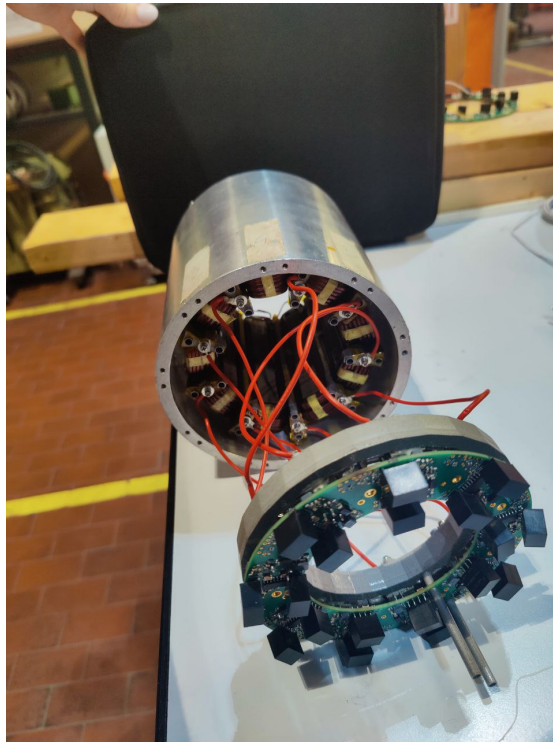


Figure 5.4: Motor connected to the nine-phase inverter

5.3 Experimental Tests on the Motor

5.3.1 Common Mode Configuration to Evaluate the Parasitic Capacitances

The motor was fed with a common mode signal to evaluate the capacitances for each of the terms. This means to only making the switches switch at a 20 kHz frequency and store the currents generated in the switching instants. Figure 5.5 shows one of the three terms fed by a three-phase inverter.

Currents shown in Figure 5.6 were stored, as well as the voltages.

The capacitance C is given by the formula:

$$C = \frac{Q}{\Delta V}$$

and the charge is:

$$Q = \int I(t) dt$$

The charge is $Q = 2.77 \times 10^{-7} C$. The capacitance is $C = 6.93 pF$

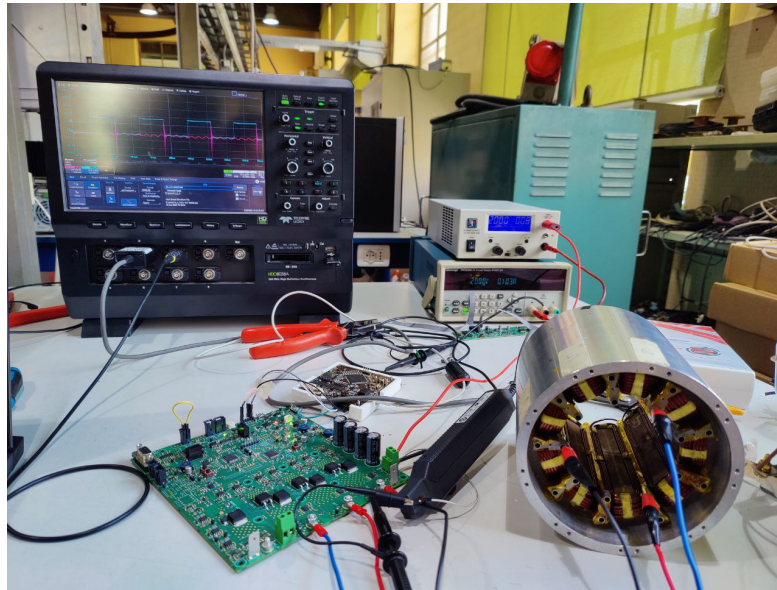


Figure 5.5: Experimental setup

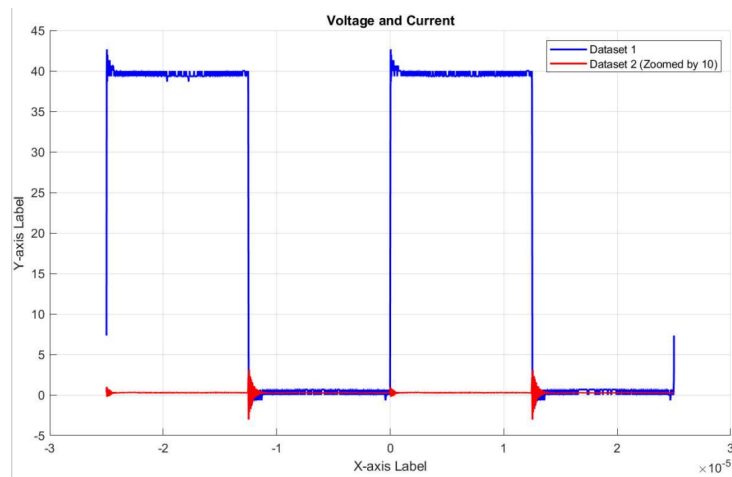


Figure 5.6: Common mode voltage and current (expanded)

Chapter 6

Conclusions

This thesis aimed to address the critical safety issues associated with parasitic capacitances and electromagnetic compatibility (EMC) in electric vehicle (EV) charging systems. By exploring the design, simulation, and testing of a nine-phase Permanent Magnet Synchronous Motor (PMSM) integrated with an inverter for bidirectional charging, the research provided significant insights and solutions for enhancing the efficiency and safety of EV chargers.

6.1 Summary of Findings

Motor Structure and Zero Torque Verification

Nine-phase PMSM with surface-mounted magnets and concentrated windings was chosen due to its ability to facilitate three-phase charging without generating torque. This configuration minimizes mechanical stress during the charging process.

FEMM 4.1 simulations and MATLAB scripts confirmed the absence of synchronous harmonics, thus validating that no torque is generated during the charging phase. Experimental tests further supported these findings, demonstrating that the rotor remains stationary under various conditions.

High-Frequency Motor Model

A high-frequency motor model was developed to simulate the behavior of the electric motor accurately. Sweep measurements and equivalent circuit modeling using passive components allowed for the implementation of the motor model in PLECS simulations. The model accurately reflected the impedance characteristics of the motor at high frequencies, which is crucial for predicting the performance and addressing potential EMC issues.

Parasitic Capacitances and Dielectric Losses

Using ANSYS, the parasitic capacitances of the motor were evaluated. The primary capacitances between different motor components were identified and quantified.

FEMM 4.2 simulations were employed to assess the dielectric losses in Cool-X devices

with various cooling liquids. The results indicated that the dielectric losses were negligible, thus ensuring the motor's efficiency and thermal management.

Prototype Assembly and Experimental Validation

A liquid-cooled version of the nine-phase motor was assembled, incorporating Cool-X devices for enhanced cooling and insulation. Initial insulation tests revealed some criticalities, which were rectified to ensure the motor's reliability.

Experimental tests on the assembled prototype validated the simulated capacitance values. The phase-to-star center capacitance measured experimentally was consistent with the simulation results, confirming the model's accuracy.

6.2 Implications for Future Research and Applications

The research presented in this thesis offers several practical implications and directions for future work:

Integrated Charging Systems: The findings confirm the feasibility of using the motor and inverter as an integrated on-board charger. This approach can reduce the number of components required in EVs, thus lowering costs and simplifying the system architecture.

Safety and EMC Compliance: Understanding and mitigating parasitic capacitances and EMC issues are crucial for the safe operation of high-power EV chargers. The developed models and experimental methods provide a foundation for further refinement and standardization in this area.

Advanced Motor Designs: The successful implementation of a nine-phase PMSM with zero torque generation during charging opens avenues for exploring other multi-phase motor configurations. Future research could focus on optimizing these designs for different types of EV applications.

6.3 Conclusion

In conclusion, this thesis has demonstrated the critical importance of addressing parasitic capacitances and EMC issues in the development of integrated drive systems for high-power EV charging. Through rigorous simulations, experimental validation, and prototype assembly, the research provides a comprehensive understanding of these challenges and presents viable solutions to enhance the performance and safety of EV chargers. The insights gained from this study are expected to contribute significantly to the advancement of reliable and sustainable electric vehicle technologies.

Appendix A

MATLAB convolution product script

This script provides the convolution product between the induction distribution produced by the permanent magnets and the magnetomotive force generated by the stator windings. It extracts synchronous harmonics that contribute to torque generation.

```
1 % Angolo elettrico e meccanico (totale)
2 OmegaE = linspace(0, 2*pi,1200);
3 OmegaM = linspace (0, 2*pi, 6000);
4
5 % Angolo di Aperura di Dente
6 AD = 0.5;
7 Pm2P = 0.9;
8
9 % Distribuzione di Induzione al traferro
10 DistrB=zeros ( size (OmegaE) );
11 IndB=find ( abs (OmegaE-pi/2)<Pm2P*pi/2 );
12 DistrB (IndB) = -1;
13 IndB=find ( abs (OmegaE-3*pi/2)<Pm2P*pi/2 );
14 DistrB (IndB) = 1;
15 DistrBtotal= repmat (DistrB ,1 ,5) ;
16
17 % Distribuzione di avvolgimenti di dente
18 DistrAvv=zeros ( size (OmegaE) );
19 DistrAvvtotal= repmat (DistrAvv ,1 ,5) ;
20 IndAvv1=find ( abs (OmegaM-pi/3)<AD/2 ); % ho considerato mezza apertura
    di dente per lato
21 DistrAvvtotal (IndAvv1) = 1;
22 IndAvv2=find ( abs (OmegaM-3*pi/3)<AD/2 );
23 DistrAvvtotal (IndAvv2) = 1;
```

```

24 IndAvv3=find( abs(OmegaM-5*pi/3)<AD/2);
25 DistrAvvtotal(IndAvv3) = 1;
26
27 % seconda sequenza di poli
28 %raddoppio per prodotto di convoluzione
29 DistrBdouble=[DistrBtotal(1:end-1) DistrBtotal];
30
31 LambdaMconv=conv(DistrAvvtotal,DistrBdouble);
32 IndLa=max(size(OmegaM));
33 MaxLaM=max(LambdaMconv);
34 LambdaM=1*LambdaMconv(IndLa:2*IndLa-1)/MaxLaM;
35
36 dime = max(size(LambdaM));
37
38 LambdaM = reshape(LambdaM,dime,1);
39 OmegaM = reshape(OmegaM,dime,1);
40 % calcola la trasformata di Fourier
41 a = fft(LambdaM);
42 % estrae la prima armonica
43 Continua=a(1)/dime;
44 Armoniche=2*abs(a(2:dime))/dime;
45
46 numarm = 1:100;
47
48 figure
49
50 subplot(2,1,1), plot(OmegaM,DistrBtotal,'b',OmegaM,DistrAvvtotal,'r')
51 ;
52 % title(['FdF= ' num2str(FdF) ' 1a= ' num2str(SIS(2))]);
53 xlabel('degrees [rad]')
54 ylabel('Windings and induction distribution')
55
56 subplot(2,1,2), bar(numarm,Armoniche(numarm),0.5,'r')
57 ylabel('Amplitude');
58 xlabel('Harmonic order')
59 grid

```


Appendix B

Mylar Datasheet



TECHNICAL DATA SHEET

Mylar® (Polyester Film)

Mylar® exhibits superior strength, heat resistance, and excellent insulating properties. The unique qualities of Mylar® are found in many consumer, high tech, and electronic markets. Mylar® Polyester Film is ideally suited for a wide range of uses such as packaging, printing, die-cutting, electronics, protective overlay, barrier protection, apparel and other industrial applications.

TYPICAL PROPERTIES of MYLAR®

Properties	Typical Value	Units	Test Method
Tensile Strength (MD)	28,000	psi	ASTM-D882
Tensile Strength (TD)	34,000	psi	ASTM-D882
Strength Elongation MD	15,000	psi	ASTM-D882
Strength F-5 TD	14,000	psi	ASTM-D882
Modulus MD	710,000	psi	ASTM-D882
Modulus TD	740,000	psi	ASTM-D882
Elongation MD	115	%	ASTM-D882
Elongation TD	92	%	ASTM-D882
Surface Roughness	38	nm	Optical Profilometer
Density	1.39	g/cc	ASTM-D1505
Viscosity	0.56	dL/g	ASTM-D4603
Yield	21,000	in ² /lb	n/a

Benefits

- Superior strength
- Heat resistance
- Insulating properties
- Good coefficient of friction (COF)
- Tear-resistant and puncture-resistant characteristics
- Excellent dimensional stability over a wide range of temperatures
- Very good resistance to most common solvents, moisture, oil, and grease
- Excellent barrier against a wide range of gases

Applications

- Packaging
- Medical
- Membrane switches
- Enhancement of LCD/Plasma/Computer Displays
- Coating for cards and discs
- Printing (when properly coated)
- Labels
- Magnetic recording media

Electrical Properties

Properties	Typical Value	Units	Test Method
Dielectric Strength AC, 20° C, .00092"	7,000	volts/mil	ASTM-D149-64
Dielectric Constant 25° C, 1kHz	3.2	n/a	ASTM-D150-81
Dissipation Factor 25° C, 1kHz	0.005	n/a	ASTM-D150-65
Volume Resistivity 25° C	1.00E+19	ohm-cm	ASTM-D257-78
Corona Threshold	V-AC	V-AC	ASTM-D2275-80

Thermal Properties

Properties	Typical Value	Units	Test Method
Melting Point	254	° C	n/a
Dimensional Stability	n/a	n/a	n/a
at 105° C MD	0.6	%	n/a
at 105° C TD	0.3	%	n/a
at 150° C MD	1.8	%	n/a
at 150° C TD	1.0	%	n/a
Specific Heat	0.28	cal/g/° C	n/a
Thermal Expansion	1.7 x 10 ⁻⁵	in/in/° C	ASTM-D696
UL94 Flame Class	94VTM-2	n/a	Slow to self extinguishing

SHAPE AVAILABLE



Contact us for manufacturers' complete material property datasheets Mylar® is a registered trademark of DuPont.

NOTE: The information contained herein are typical values intended for reference and comparison purposes only. They should NOT be used as a basis for design specifications or quality control. Contact us for manufacturers' complete material property datasheets. All values at 73°F (23°C) unless otherwise noted.

Appendix C

MATLAB Bode plot approximation script, phase-to-star center impedance

This script permits to have a transfer function whose Bode plot is similar to the one obtained with sweep measurement of the phase-to-star center motor impedance.

```
1 clear all
2 clc
3
4 % Given frequency and impedance data
5 frequency = [10, 50, 1000, 5000, 10000, 25000, 50000, 75000, 100000,
6             ...
7             200000, 300000, 400000, 500000, 600000, 700000, 800000,
8             900000, 1000000];
9 impedance = [1.31e-01, 3.41e-01, 6.25e+00, 2.93e+01, 5.22e+01, 1.05e
10             +02, ...
11             1.79e+02, 2.45e+02, 3.06e+02, 5.28e+02, 7.49e+02, 9.91e
12             +02, ...
13             1.27e+03, 1.61e+03, 1.96e+03, 2.26e+03, 2.51e+03, 2.74e
14             +03];
15
16 % Experimental phase data
17 experimental_phase = [29.603, 69.981, 85.951, 78.93, 73.699, 70.275,
18                      68.951, ...
19                      68.035, 67.344, 65.394, 63.411, 60.715, 56.966,
20                      50.979, ...
```

```

14 |                                     42.053, 31.732, 21.611, 10.542];
15 |
16 | % Convert impedance to dB
17 | impedance_dB = 20 * log10(impedance);
18 |
19 | % Initial estimates for transfer function parameters
20 | K = 0.001;
21 | omega_z = 2 * pi * 10; % Initial estimate for zero at 10 Hz
22 |
23 | % Create the transfer function
24 | num = [K, K * omega_z];
25 | den = [1];
26 | sys = tf(num, den);
27 |
28 | % Compute Bode plot
29 | [mag, phase, w] = bode(sys, 2 * pi * frequency);
30 | mag = squeeze(mag);
31 | phase = squeeze(phase);
32 |
33 | % Equivalent bipole components
34 | R = 0.06283;
35 | L = 0.001;
36 |
37 | % Create the transfer function for the equivalent bipole
38 | num_bipole = [L, R];
39 | den_bipole = [1];
40 | sys_bipole = tf(num_bipole, den_bipole);
41 |
42 | % Compute Bode plot for the equivalent bipole
43 | [mag_bipole, phase_bipole, w_bipole] = bode(sys_bipole, 2 * pi *
44 |     frequency);
45 | mag_bipole = squeeze(mag_bipole);
46 | phase_bipole = squeeze(phase_bipole);
47 |
48 | % Define the frequency range for analysis
49 | frequencies = logspace(0, 6, 500);
50 | omega_s = 2 * pi * frequencies;
51 |
52 | % Plot experimental data and simulated data
53 | figure;
54 | % Magnitude plot
55 | subplot(2, 1, 1);
56 | semilogx(frequency, impedance_dB, 'o-', 'Color', [0 0 1], '
57 |     MarkerFaceColor', [0 0 1], 'MarkerEdgeColor', 'k', 'LineWidth',
58 |     1.5); % Experimental data
59 | hold on;
60 | semilogx(frequency, 20*log10(mag), 'c--', 'LineWidth', 1.5); %
61 |     Simulated data

```

```

59 semilogx(frequency, 20*log10(mag_bipole), '-', 'Color', [0 0.5 0], '
    LineWidth', 1.5); % Bipole data
60 xlabel('Frequency (Hz)');
61 ylabel('Magnitude (dB)');
62 title('Magnitude Bode Plot');
63 legend('Experimental', 'Simulated', 'Synthesized RLC');
64 xlim([1e1 max(frequencies)]); % Set x-axis limit
65 grid on;
66
67 % Phase plot
68 subplot(2, 1, 2);
69 semilogx(frequency, experimental_phase, 'o-', 'Color', [0 0 1], '
    MarkerFaceColor', [0 0 1], 'MarkerEdgeColor', 'k', 'LineWidth',
    1.5); % Experimental phase data
70 hold on;
71 semilogx(frequency, phase, 'c--', 'LineWidth', 1.5); % Simulated data
72 semilogx(frequency, phase_bipole, '-', 'Color', [0 0.5 0], 'LineWidth
    ', 1.5); % Bipole data
73 xlabel('Frequency (Hz)');
74 ylabel('Phase (degrees)');
75 title('Phase Bode Plot');
76 legend('Experimental', 'Simulated', 'Synthesized RLC');
77 xlim([1e1 max(frequencies)]); % Set x-axis limit
78 grid on;
79
80 % Adjust layout
81 sgtitle('Frequency Response Comparison');

```

Appendix D

MATLAB Bode plot approximation script, phase-to-housing impedance

This script permits to have a transfer function whose Bode plot is similar to the one obtained with sweep measurement of the phase-to-ground motor impedance.

```
1
2
3 clear all;
4 clc;
5
6 % Given frequency, impedance, and phase data
7 frequency = [10, 50, 100, 500, 1000, 5000, 10000, 25000, 50000,
8             75000, ...
9             100000, 200000, 300000, 400000, 500000, 600000, 700000,
10            800000, 900000, 1000000];
11 impedance = [3.04e+07, 1.80e+07, 1.97e+06, 6.61e+05, 3.22e+05, 6.18e
12             +04, ...
13             3.09e+04, 1.24e+04, 6.13e+03, 3.99e+03, 2.90e+03, 1.19e
14             +03, ...
15             5.73e+02, 4.60e+02, 7.32e+02, 1.14e+03, 1.58e+03, 1.91e
16             +03, ...
17             2.08e+03, 2.15e+03];
18 phase = [-87.45, 4.496, -86.572, -94.062, -89.169, -89.343, -89.35,
19          -89.264, ...
20          -89.019, -88.223, -87.308, -79.726, -56.97, -6.122, 22.392,
21          26.823, ...
22          20.103, 8.592, -2.733, -13.218];
```

```

17 % Convert impedance to dB
18 impedance_dB = 20 * log10(impedance);
19
20 % Convert frequency to rad/s
21 omega = 2 * pi * frequency;
22
23 % Define the estimated transfer function
24 K = 1e3; % Gain
25 z1 = 1e6; % Zero 1
26 z2 = 1e5; % Zero 2
27 p1 = 1e3; % Pole 1
28 p2 = 1e4; % Pole 2
29
30 num = K * [1 (z1+z2) (z1*z2)];
31 den = [1 (p1+p2) (p1*p2)];
32
33 sys = tf(num, den);
34
35 % Synthesize RLC Circuit using Foster Method
36
37 % Step 1: Partial Fraction Expansion
38 A = K * ((z1*z2*p1) / (p1 - p2));
39 B = K * ((z1*z2*p2) / (p2 - p1));
40
41 % Step 2: Calculate R, L, and C values for the synthesized RLC
    circuit
42 R1 = A;
43 C1 = 1 / (p1 * R1);
44 L1 = R1 / p1;
45
46 R2 = B;
47 C2 = 1 / (p2 * R2);
48 L2 = R2 / p2;
49
50 % Define the frequency range for analysis
51 frequencies = logspace(0, 6, 500);
52 omega_s = 2 * pi * frequencies;
53
54 % Calculate the impedance of the synthesized RLC circuit
55 Z1 = R1 + 1 ./ (1j * omega_s * C1) + 1j * omega_s * L1;
56 Z2 = R2 + 1 ./ (1j * omega_s * C2) + 1j * omega_s * L2;
57 Z_total = 1 ./ (1 ./ Z1 + 1 ./ Z2);
58
59 % Calculate the transfer function magnitude and phase
60 H_mag = abs(1 ./ Z_total);
61 H_phase = angle(1 ./ Z_total);
62
63 % Plot all three curves on the same plot
64 figure;

```

```

65
66 % Magnitude plot
67 subplot(2, 1, 1);
68 semilogx(frequency, impedance_dB, 'o-', 'Color', [0 0 1], '
    MarkerFaceColor', [0 0 1], 'MarkerEdgeColor', 'k', 'LineWidth',
    1.5);
69 hold on;
70 [mag, ~, ~] = bode(sys, omega);
71 mag = squeeze(mag);
72 semilogx(frequency, 20*log10(mag), 'c--', 'LineWidth', 1.5); %
    Estimated data
73 semilogx(frequencies, H_mag_offset_dB, '-', 'Color', [0 0.5 0], '
    LineWidth', 1.5); % Synthesized RLC circuit with offset
74 xlabel('Frequency (Hz)');
75 ylabel('Magnitude (dB)');
76 title('Bode Plot of Impedance Magnitude');
77 legend('Experimental', 'Estimated', 'Synthesized RLC');
78 xlim([1e2 max(frequencies)]); % Set x-axis limit
79 grid on;
80
81 % Phase plot
82 subplot(2, 1, 2);
83 semilogx(frequency, phase, 'o-', 'Color', [0 0 1], 'MarkerFaceColor',
    [0 0 1], 'MarkerEdgeColor', 'k', 'LineWidth', 1.5);
84 hold on;
85 [~, phase_est, ~] = bode(sys, omega);
86 phase_est = squeeze(phase_est);
87 semilogx(frequency, phase_est, 'c--', 'LineWidth', 1.5); % Estimated
    data
88 semilogx(frequencies, rad2deg(H_phase), '-', 'Color', [0 0.5 0], '
    LineWidth', 1.5); % Synthesized RLC circuit
89 xlabel('Frequency (Hz)');
90 ylabel('Phase (degrees)');
91 title('Bode Plot of Phase');
92 legend('Experimental', 'Estimated', 'Synthesized RLC');
93 xlim([1e2 max(frequencies)]); % Set x-axis limit
94 grid on;
95
96 % Adjust layout
97 sgtitle('Frequency Response Comparison');

```

Appendix E

MATLAB Bode plot approximation script, star center-to-housing impedance

This script permits to have a transfer function whose Bode plot is similar to the one obtained with sweep measurement of the star center-to-housing motor impedance.

```
1
2 % Clear workspace and command window
3 clear all;
4 clc;
5
6 % EXPERIMENTAL DATA
7
8 % Given frequency, impedance, and phase data
9 frequency = [10, 50, 100, 500, 1000, 5000, 10000, 25000, 50000,
10             75000, ...
11             100000, 200000, 300000, 400000, 500000, 600000, 700000,
12             800000, 900000, 1000000];
13 impedance = [3.03e+07, 4.32e+06, 6.19e+06, 6.42e+05, 3.53e+05, 6.19e
14             +04, ...
15             3.10e+04, 1.25e+04, 6.27e+03, 4.18e+03, 3.13e+03, 1.56e
16             +03, ...
17             1.02e+03, 7.52e+02, 5.88e+02, 4.82e+02, 4.14e+02, 3.77e
18             +02, ...
19             3.65e+02, 3.60e+02];
20 phase = [-90.328, -44.354, -45.703, -90.149, -89.439, -89.398,
21          -89.381, -89.448, ...
22          -89.5, -89.382, -89.325, -89.038, -88.375, -87.404, -85.519,
23          -82.563, ...
```



```

17         -78.644, -74.244, -71.418, -72.076];
18
19 % Convert impedance to dB
20 impedance_dB = 20 * log10(impedance);
21
22 % Convert frequency to rad/s
23 omega_exp = 2 * pi * frequency;
24
25 % APPROXIMATED TRANSFER FUNCTION
26
27 % Define a transfer function
28 K = 1.8e9;
29 z1 = 1;
30 p1 = 1e1;
31 p2 = 5e2;
32
33 num = K * [1 z1];
34 den = [1 (p1+p2) (p1*p2)];
35
36 sys = tf(num, den);
37
38 % SYNTHESIZED RLC CIRCUIT
39
40 % Define component values for the RLC circuit
41 R1 = -3.3061e7; % Ohms (ideal negative resistor for illustration)
42 C1 = 1 / (10 * abs(R1)); % Farads, assuming the magnitude of R1 for
    calculation
43
44 R2 = 1.8337e9; % Ohms
45 L2 = 3.6674e6; % Henry
46
47 % Define the frequency range for analysis
48 frequencies = logspace(0, 6, 500); % Frequency range from 10^0 to
    10^6 Hz
49 omega = 2 * pi * frequencies; % Angular frequency
50
51 % Calculate the impedance of the RC parallel circuit
52 Z1 = 1 ./ (1/R1 + 1./(1j * omega * C1));
53
54 % Calculate the impedance of the RL series circuit
55 Z2 = R2 + 1j * omega * L2;
56
57 % Total impedance
58 Z_total = Z1 + Z2;
59
60 % Calculate the transfer function magnitude and phase
61 H_mag = abs(1 ./ Z_total);
62 H_phase = angle(1 ./ Z_total);
63

```

```

64 % Define color for darker green
65 darker_green = [0 0.5 0];
66
67 % Plot all three curves on the same plot
68 figure;
69
70 % Magnitude plot
71 subplot(2, 1, 1);
72 semilogx(frequency, impedance_dB, 'o-', 'Color', [0 0 1], '
    MarkerFaceColor', [0 0 1], 'MarkerEdgeColor', 'k', 'LineWidth',
    1.5);
73 hold on;
74 [mag, ~, ~] = bode(sys, omega_exp);
75 mag = squeeze(mag);
76 semilogx(frequency, 20*log10(mag), 'c--', 'LineWidth', 1.5); %
    Estimated data
77 semilogx(frequencies, H_mag_offset_dB, '-', 'Color', darker_green, '
    LineWidth', 1.5); % Synthesized RLC circuit with offset
78 xlabel('Frequency (Hz)');
79 ylabel('Magnitude (dB)');
80 title('Bode Plot of Impedance Magnitude');
81 legend('Experimental', 'Estimated', 'Synthesized RLC');
82 xlim([1e2 max(frequencies)]); % Set x-axis limit
83 grid on;
84
85 % Phase plot
86 subplot(2, 1, 2);
87 semilogx(frequency, phase, 'o-', 'Color', [0 0 1], 'MarkerFaceColor',
    [0 0 1], 'MarkerEdgeColor', 'k', 'LineWidth', 1.5);
88 hold on;
89 [~, phase_est, ~] = bode(sys, omega_exp);
90 phase_est = squeeze(phase_est);
91 semilogx(frequency, phase_est, 'c--', 'LineWidth', 1.5); % Estimated
    data
92 semilogx(frequencies, rad2deg(H_phase), '-', 'Color', darker_green, '
    LineWidth', 1.5); % Synthesized RLC circuit
93 xlabel('Frequency (Hz)');
94 ylabel('Phase (degrees)');
95 title('Bode Plot of Phase');
96 legend('Experimental', 'Estimated', 'Synthesized RLC');
97 xlim([1e2 max(frequencies)]); % Set x-axis limit
98 grid on;
99
100 % Adjust layout
101 sgtitle('Frequency Response Comparison');

```

Bibliography

- [1] Andrea Malan. «Sub-25,000 euro EVs can be built in Europe, environment group says». In: *Automotive News Europe* (2023) (cit. on p. 1).
- [2] European Union. «New registrations of electric vehicles in Europe». In: *European Environmental Agency* (2023) (cit. on p. 1).
- [3] Chan-Ho Kim, Han-Joon Yoon, and Sang-Yong Jung. «Parasitic Capacitance Calculation by Electric Field Decomposition Method for Electric Motor». In: Nov. 2022, pp. 1–4. DOI: 10.1109/ICEMS56177.2022.9982864 (cit. on p. 5).
- [4] IEA Paris. *Global EV Outlook 2021*. Tech. rep. available online with Licence CC BY 4.0. IEA Paris, 2021. URL: <https://www.iea.org/reports/global-ev-outlook-2021> (cit. on p. 6).
- [5] Laura Jones; Kathryn Lucas-Healey; Björn Sturmborg; Hugo Temby and Monirul Islam. *The A to Z of V2G A comprehensive analysis of vehicle-to-grid technology worldwide*. Tech. rep. available online. Australian Technical University; ARENA, Jan. 2021. URL: <https://arena.gov.au/assets/2021/01/revs-the-a-to-z-of-v2g.pdf> (cit. on p. 6).
- [6] *Electric vehicle conductive charging system - Part 1: General requirements*. BSI Standards Limited 2019, 2017. URL: <https://webstore.iec.ch/publication/33644> (cit. on p. 6).
- [7] *Plugs, socket-outlets, vehicle connectors and vehicle inlets - Conductive charging of electric vehicles - Part 1: General requirements*. BSI Standards Limited 2019, May 2022. URL: <https://webstore.iec.ch/publication/59922> (cit. on p. 7).
- [8] *Plugs, socket-outlets, vehicle connectors and vehicle inlets - Conductive charging of electric vehicles - Part 2: Dimensional compatibility requirements for AC pin and contact-tube accessories*. BSI Standards Limited 2019, 2022. URL: <https://webstore.iec.ch/publication/64364> (cit. on p. 7).

- [9] Simon Luyten, Niels Leemput, Frederik Geth, Juan Van Roy, Jeroen Büscher, and Johan Driesen. «Standardization of conductive AC charging infrastructure for electric vehicles». In: *22nd International Conference and Exhibition on Electricity Distribution (CIRED 2013)*. 2013, pp. 1–4. DOI: 10.1049/cp.2013.0751 (cit. on p. 8).
- [10] *Electric vehicle conductive charging system - Part 23: DC electric vehicle charging station*. BSI Standards Limited 2019, 2014. URL: <https://webstore.iec.ch/publication/6032> (cit. on p. 8).
- [11] *Electric vehicle conductive charging system - Part 24: Digital communication between a d.c. EV charging station and an electric vehicle for control of d.c. charging*. BSI Standards Limited 2019, 2014. URL: <https://webstore.iec.ch/publication/6033> (cit. on p. 8).
- [12] *Plugs, socket-outlets, vehicle connectors and vehicle inlets - Conductive charging of electric vehicles - Part 3: Dimensional compatibility requirements for DC and AC/DC pin and contact-tube vehicle couplers*. BSI Standards Limited 2019, 2022. URL: <https://webstore.iec.ch/publication/59923> (cit. on p. 8).
- [13] «Effects of Current on Human Beings and Livestock». In: *IEC 60479-1 (2005)* (cit. on p. 11).
- [14] «Occupational Safety and Health Administration (OSHA) Guidelines». In: *OSHA (2021)*. URL: <https://www.osha.gov> (cit. on p. 11).
- [15] «Electric Motors - European Commission». In: *European Commission (2021)*. URL: <https://energy-efficient-products.ec.europa.eu> (cit. on p. 11).
- [16] «Motor Enclosures: What You Need to Know». In: *Pumps & Systems (2003)*. URL: <https://www.pumpsandsystems.com> (cit. on p. 12).
- [17] «Research on Analysis and Suppression Methods of the Bearing Current for Electric Vehicle Motor Driven by SiC Inverter». In: *Energies (2024)*. URL: <https://www.mdpi.com> (cit. on p. 12).
- [18] R. Bojoi, A. Cavagnino, A. Tenconi, A. Tassarolo, and S. Vaschetto. «Multi-phase electrical machines and drives in the transportation electrification». In: *2015 IEEE 1st International Forum on Research and Technologies for Society and Industry Leveraging a better tomorrow (RTSI)*. 2015, pp. 205–212. DOI: 10.1109/RTSI.2015.7325099 (cit. on p. 12).
- [19] *Voltage characteristics of electricity supplied by public electricity networks*. 2023. URL: <https://bsol-bsigroup-com.ezproxy.biblio.polito.it/Search/Search?searchKey=50160&OriginPage=Header+Search+Box&autoSuggestion=false> (cit. on p. 17).

- [20] *Voltage characteristics of electricity supplied by public electricity networks*. 2022. URL: <https://www.certifico.com/impianti/documenti-impianti/340-documenti-impianti-cei/16440-cei-0-21-2022> (cit. on p. 17).
- [21] «LFP Vs NMC Battery: Complete Comparison Guide». In: <https://www.ecolithiumbattery.com/...> (cit. on p. 19).
- [22] *Classificazione dei sistemi elettrici*. Mar. 2019. URL: <https://www.certifico.com/impianti/361-news-impianti/7909-classificazione-dei-sistemi-elettrici> (cit. on p. 19).
- [23] supplier’s website. URL: https://www.wolfspeed.com/trusted-silicon-carbide-partner/?utm_campaign=power_general-power_considerfy24&utm_source=google&utm_medium=cpc&utm_term=brand&utm_content=WS00823&gad=1 (cit. on p. 20).
- [24] Luis De Sousa, Benedicte Silvestre, and Boris Bouchez. «A combined multiphase electric drive and fast battery charger for Electric Vehicles». In: *2010 IEEE Vehicle Power and Propulsion Conference*. 2010, pp. 1–6. DOI: 10.1109/VPPC.2010.5729057 (cit. on pp. 22, 23).
- [25] Ivan Subotic, Nandor Bodo, Emil Levi, and Martin Jones. «Onboard Integrated Battery Charger for EVs Using an Asymmetrical Nine-Phase Machine». In: *IEEE Transactions on Industrial Electronics* 62.5 (2015), pp. 3285–3295. DOI: 10.1109/TIE.2014.2345341 (cit. on p. 23).
- [26] free software available online. URL: <https://www.femm.info/wiki/HomePage> (cit. on p. 24).
- [27] Yongchang Zhang, Jianguo Zhu, Wei Xu, and Youguang Guo. «A Simple Method to Reduce Torque Ripple in Direct Torque-Controlled Permanent-Magnet Synchronous Motor by Using Vectors With Variable Amplitude and Angle». In: *IEEE Transactions on Industrial Electronics* 58.7 (2011), pp. 2848–2859. DOI: 10.1109/TIE.2010.2076413 (cit. on p. 27).
- [28] P. L. Alger and H. W. Samson. «Shaft Currents in Electric Machines». In: *Transactions of the American Institute of Electrical Engineers* XLIII (1924), pp. 235–245. DOI: 10.1109/T-AIEE.1924.5060981 (cit. on p. 34).
- [29] Aldo Boglietti, Andrea Cavagnino, and Mario Lazzari. «Experimental High-Frequency Parameter Identification of AC Electrical Motors». In: *IEEE Transactions on Industry Applications* 43.1 (2007), pp. 23–29. DOI: 10.1109/TIA.2006.887313 (cit. on pp. 35, 36, 40).
- [30] S. Ogasawara and H. Akagi. «Modeling and damping of high-frequency leakage currents in PWM inverter-fed AC motor drive systems». In: *IEEE Transactions on Industry Applications* 32.5 (1996), pp. 1105–1114. DOI: 10.1109/28.536872 (cit. on p. 35).

- [31] E. Carpaneto A. Boglietti. «An Accurate Induction Motor High-Frequency Model for Electromagnetic Compatibility Analysis». In: *Electric Power Components and Systems* 29.3 (2001), pp. 191–209. DOI: 10.1080/153250001300006626. eprint: <https://doi.org/10.1080/153250001300006626>. URL: <https://doi.org/10.1080/153250001300006626> (cit. on p. 36).
- [32] *DuPont™ Kapton® FPC*. DuPont. June 2019 (cit. on p. 37).
- [33] Claudio Beccari. *Sintesi dei circuiti passivi*. CLUT, 1989 (cit. on p. 48).